Concerted single-nanowire absorption and emission spectroscopy: Explaining the origin of the size-dependent Stokes shift in single cadmium selenide nanowires

F. Vietmeyer, R. Chatterjee, M. P. McDonald, and M. Kuno

Phys. Rev. B **91**, 085422 — Published 23 February 2015

DOI: 10.1103/PhysRevB.91.085422

Concerted single nanowire absorption and emission spectroscopy: Explaining the origin of the size-dependent Stokes shift in single cadmium selenide nanowires

F. Vietmeyer[1†], R. Chatterjee[2†], M. P. McDonald[2] and M. Kuno[2]*

[1]*JILA University of Colorado, Boulder, CB440, Boulder CO 80525*
[2]*Department of Chemistry and Biochemistry, University of Notre Dame, Notre Dame, Indiana 46556, USA*
[†]*F. Vietmeyer and R. Chatterjee contributed equally to this work*
***mkuno@nd.edu**

PACS number(s): 42.70.-a, 62.23.Hj, 73.23.f, 71.35.-y

ABSTRACT

Concerted single nanowire (NW) absorption and emission spectroscopies have been used to measure Stokes shifts in the optical response of individual CdSe nanowires. Obtained spectra are free of inhomogeneous broadening inherent to ensemble measurements. They reveal, for the first time, apparent size-dependent NW Stokes shifts with magnitudes on the order of 30 meV. Given that an effective mass model previously used to explain CdSe nanowire excited state progressions predicts no sizable emission Stokes shift, we have investigated modifications to the theory to rationalize their existence. This has entailed better accounting for the effects of crystal field splitting on NW band edge states. What results are important changes to the spectroscopic assignment of NW band edge transitions that arise from the crossing of hole levels. Furthermore, these modifications simultaneously predict Stokes shifts with size-dependent magnitudes up to 20 meV. However, quantitative agreement with experiment is only achieved by accounting for the role of exciton trap states. Consequently, we conclude that CdSe NW Stokes shifts contain both intrinsic and extrinsic contributions—the latter arising from band edge

exciton potential energy fluctuations. At a broader level, these concerted absorption and emission measurements have provided detailed insight into the electronic structure of CdSe NWs, beyond what could be obtained using either single particle absorption or emission spectroscopies alone.

I. INTRODUCTION

II-VI semiconductor nanostructures are currently some of the most widely studied systems in modern nanoscience. This is due to their distinctive size- and shape-dependent optical and electrical properties.[1,2] Recent advances in the synthesis of high quality one-dimensional (1D) II-VI nanostructures have led to extensive studies of their optoelectronic properties[3,4,5,6,7,8] as well as their use in diverse applications.[9,10] In this regard, the anisotropic shape of these materials allows for efficient charge transport while quantum confinement leads to tunable electronic properties. Both make II-VI nanorods (NRs) and nanowires (NWs) useful for photoconductive devices.[11,12] Furthermore, their linearly polarized emission[13] makes them useful in devices such as light emitting diodes and sensors.[14]

A thorough understanding of their photophysics, however, is essential to fully exploiting them in applications. This, in turn, requires developing a better understanding of NR and NW electronic structure, which is well reflected in their linear absorption and emission spectra. Consequently, concerted absorption and emission measurements offer an effective means for probing confinement as well as dielectric environment induced variations of nanostructure electronic properties.

A notable example where such correlated measurements have been critical to establishing the electronic structure of low dimensional materials involves colloidal CdSe quantum dots

(QDs).[15,16] Specifically, detailed ensemble absorption and emission studies have previously led to excellent agreement between theoretically-derived transition energies and experimental excitation spectra. This has led to spectroscopic assignment of QD excitonic transitions as well as to observations of characteristic avoided crossings in their size-dependent spectra.[16]

Such studies have also been critical in explaining unusual properties of the emission. This includes the existence of both resonant and non-resonant Stokes shifts, their widely differing magnitudes and their characteristic temperature-dependencies.[17] Consequently, joint absorption and emission measurements have established that the photoluminescence (PL) from CdSe QDs arises from intrinsic fine structure states, resulting from crystal field splitting, nanocrystal shape asymmetry and the electron-hole exchange interaction.[17,18] They do not appear to originate from extrinsic, surface-related states.[19,20]

Interestingly, the advent of shape-controlled syntheses has led to analogous observations of emission Stokes shifts in 1D materials. Values as high as ~100 meV have been seen in CdSe NRs[13] while values on the order of ~50 meV have been found for PbSe and CdSe NWs.[21,22,23] However, little work has been done to establish the intrinsic or extrinsic origin of these shifts given the inability of ensemble absorption and emission measurements to capture the true underlying optical response of these materials. This stems, in part, from the structural, chemical and environmental heterogeneities inherent to chemically-synthesized ensembles, which exhibit size and shape polydispersities.

Single particle absorption and emission studies thus offer a way to circumvent this limitation. In this manner, exquisite details of NR or NW electronic structure can be revealed. While single particle *emission* spectroscopy is a well-established technique,[24,25,26] corresponding absorption measurements are difficult due to the relatively low absorption efficiencies of individual particles. Namely, NW cross sections on the order of $\sigma \sim 10^{-12} - 10^{-11}$ cm^2 μm^{-1} imply that only ~0.01 – 0.1% of incident light is attenuated in a single particle absorption experiment.[27,28]

Recently, we have demonstrated the use of single particle, spatial modulation microscopy to acquire size-dependent extinction spectra of individual CdSe NWs[29] and gold nanoparticles.[30] We have also used this technique to acquire chirality-dependent spectra of single walled carbon nanotubes.[30] In the case of CdSe NWs, we have assigned observed transitions to predictions of a 6-band effective mass model.[29] This has, in turn, revealed the existence of room temperature 1D excitons[29] as well as the size-dependent interplay between quantum confinement, dielectric contrast and carrier electrostatic interactions in NWs. These spectroscopic assignments have been further corroborated by additional single NW absorption polarization anisotropy measurements we have made.[31]

In the current study, we use concerted single NW absorption and emission experiments to develop further insight into the electronic structure of CdSe NWs. These combined measurements have enabled us to establish the existence of size-dependent Stokes shifts in CdSe NWs with radii $a \sim 2$–7 nm. The presence of such Stokes shifts is notable since they are not predicted by an effective mass theory previously used to describe their size-dependent absorption spectra[29] or their corresponding absorption polarization anisotropies.[31]

In what follows, we rationalize the existence of a CdSe NW Stokes shift. Section II provides experimental details of our correlated single NW absorption and emission measurements. Section III describes work to explicitly incorporate the effects of crystal field splitting into the effective mass theory previously used to describe CdSe NW electronic states. Subsequent implications on the assignment of NW optical transitions are discussed. Finally, Section IV quantitatively explains the magnitude of observed Stokes shifts, by including contributions from band edge exciton potential energy fluctuations. Section V summarizes the study.

II. EXPERIMENT AND RESULTS

A. Nanowire sample characterization

Three CdSe NW ensembles with mean radii of $\langle a \rangle$ ~2.5, ~3.7 and ~5.0 nm, were prepared using solution-liquid-solid (SLS) growth.[5,6,32] For $\langle a \rangle$ ~ 2.5 nm samples, a typical synthesis entailed mixing cadmium oxide (25 mg, 0.19 mmol), myristic acid (0.662 g, 2.9 mmol) and trioctylphosphine oxide (0.5 g, 1.3 mmol) in a three neck flask. The contents were degassed at 100 °C for 50 min, whereupon the temperature was raised to 250 °C under nitrogen. A solution of 1 M trioctylphosphine selenide (25 μL, 25 μmol), 0.2 mL trioctylphosphine and 1 mM bismuth trichloride in acetone (25 μL, 25 nmol) was then injected into the vessel to initiate NW growth. After 2 minutes, the reaction was quenched through rapid cooling. Resulting NWs were recovered by centrifuging the reaction mixture. Excess trioctylphosphine oxide was removed by washing the NW product 3-4 times with a 70:30 toluene:methanol mixture. Recovered NWs were then stored in toluene. Additional descriptions of SLS NW growth as well as details of the synthesis of $\langle a \rangle$ ~3.7 and ~5.0 nm wires can be found in the literature[6,32,33,34,35] and in the Appendix.

Figure 1 shows low and high magnification TEM images of representative $\langle a \rangle$ ~2.5 nm CdSe NWs. The wires possess narrow diameters as well as crystalline zincblende/wurtzite (ZB/W) phase admixtures.[23] These phase admixtures appear in high resolution TEM images as twinning-induced "zig-zag" lattice fringes in ⟨110⟩-oriented nanowires. For [111] ZB growth direction NWs, fringes follow their longitudinal growth axis, as illustrated in **Figure 1 (b)**.[33] Additional

TEM micrographs of $\langle a \rangle$ ~3.7 and ~5.0 nm CdSe NWs can be found in the Appendix (**Figures 6** and **7**).

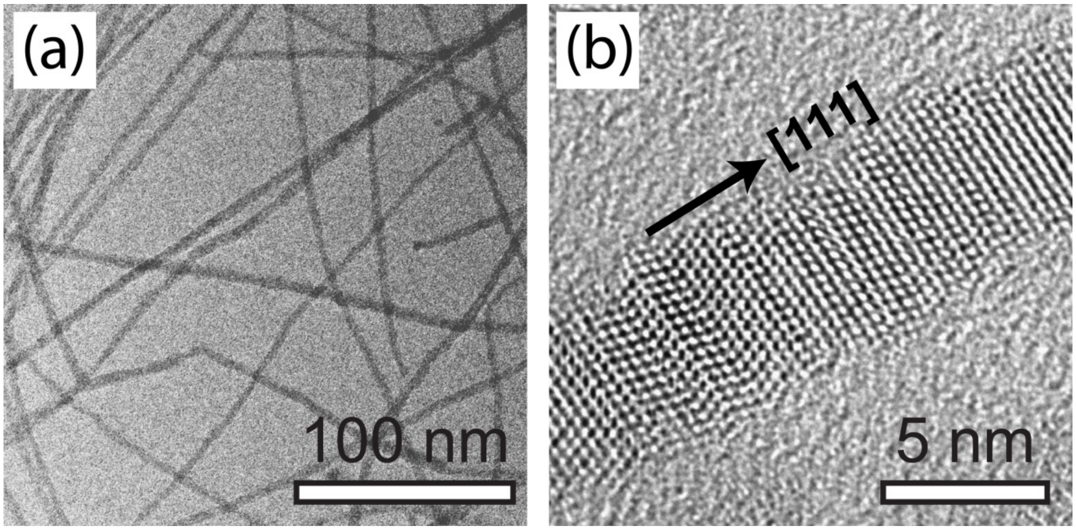

FIG. 1. (a) Low magnification TEM image of an $\langle a \rangle$ ~2.5 nm CdSe NW ensemble. (b) High magnification TEM image of an individual [111] growth direction CdSe NW, exhibiting ZB/W "zig-zag" fringes along its longitudinal axis.

B. Single nanowire absorption and emission spectroscopy

Single nanowire extinction spectra were acquired using a supercontinuum light source (Fianium, SC450). For most measurements, a home-built double prism monochromator (spectral range: 450-800 nm) was used to disperse the laser's output. This resulted in a prolate spot (~1 μm long axis). Later measurements employed a dispersive, dual crystal acousto-optic tunable filter (AOTF, Fianium). This resulted in a tighter, diffraction-limited circular spot. In all cases, the dispersed supercontinuum was passed through a sheet polarizer before being split into signal (30%) and reference (70%) beams with a 70/30 beam splitter.

Samples were prepared by drop-casting dilute nanowire suspensions onto flamed glass coverslips. Samples were then placed atop an open-loop piezoelectric modulator (Nanonics), supported by a 3-axis closed-loop piezo stage (Physik Instrumente) which was, in turn, coupled to a 2-axis manual micrometer stage (Semprex). A high numerical aperture dry objective (0.95

NA, Nikon) focused the signal beam onto the sample with the polarization parallel to the NW growth axis. Low excitation intensities (I ≤ 400 W/cm^2) were used since prior single NW absorption measurements have illustrated that NW excitonic transitions saturate when intensities exceed ~400 W/cm^2.[29] Transmitted light was collected with a second high NA, dry objective (0.75 NA, Zeiss), oriented collinear to the first. The light was then focused onto the signal channel of an autobalanced photodiode (Newport, Nirvana 2007) with the reference beam focused onto the reference channel of the same detector.

Extinction measurements were performed by moving the single NW in and out of the focused signal beam at 750 Hz. Subsequent changes in the transmitted light intensity were measured using lock-in detection (Stanford Research Systems, SR830). Both signal and reference readings then enabled wavelength-dependent, single NW extinction cross sections to be extracted. Additional details about these single NW absorption experiments can be found in Refs. 29 and 31.

Single NW PL spectra were obtained by exciting individual wires with the linearly polarized output of either a 532 nm (Power Technology Inc.) or a 473 nm (Oxxius) diode laser. The excitation spot was first enlarged to ~30 μm diameter by placing a f = 40 cm lens prior to the focusing objective's back aperture. Typical excitation intensities were I ~ 400 W/cm^2. NW emission was collected with the same objective and was passed through a 570 nm long pass filter (Chroma) before being imaged with a CCD/imaging spectrometer combination (DVC/Acton). All emission spectra were corrected for the spectrometer's grating response.

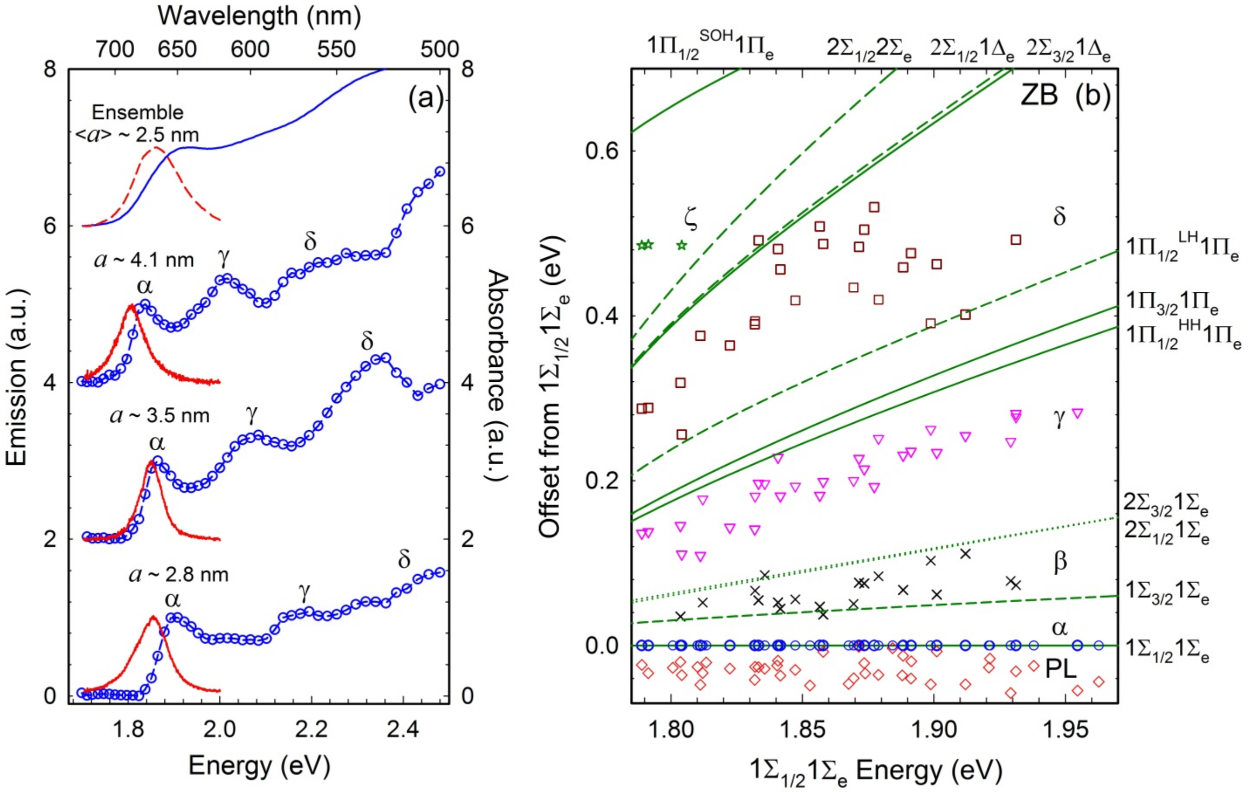

FIG. 2. (a) Absorption and emission spectra of three individual CdSe NWs with different radii (open blue circles and solid red lines respectively). Also shown is the corresponding ensemble absorption (solid blue line) and emission (dashed red line) spectra. Data offset for clarity. (b) Absorption and emission transition energies (symbols) plotted for different NW radii as functions of experimental $1\Sigma_{1/2}1\Sigma_e$ (α) energies. Solid, dashed and dotted lines represent predictions of an effective mass model developed for ZB NWs. The model assumes that the dielectric constants of the wire and the surrounding medium are $\varepsilon_s = 6.1$ and $\varepsilon_m = 2.0$ respectively.

Figure 2 (a) shows representative single NW absorption (open blue circles) and emission (solid red curves) spectra obtained from these measurements. Spectra for three different NW radii (a ~2.8, 3.5 and 4.1 nm) are shown. For comparison purposes, the corresponding ensemble ($\langle a \rangle$ ~ 2.5 nm) absorption (solid blue curve) and emission (dashed red curve) spectra have been provided. Due to their small size, single NW extinction spectra essentially represent their absorption since scattering accounts for less than 5% of the extinguished light.[27]

All single-wire spectra exhibit resonances otherwise hidden in the corresponding ensemble absorption spectrum. Specifically, three transitions, labeled α, γ and δ, are apparent in the wires shown in **Figure 2 (a)**. A fourth transition, β, is not always evident but occasionally appears as a high energy shoulder to α. Furthermore, in large diameter NWs, a 5th transition, ζ, is occasionally observed. Transition energies are extracted by fitting each spectrum to a sum of Gaussians.[29] **Figure 2 (b)** summarizes these energies by plotting experimentally-determined α, β, γ, δ, and ζ transition energies, across 43 individual NWs, all as functions of α's energy.

We have previously accounted for the size-dependent evolution of these transitions[4,29,31] using results from a 6-band effective mass model, first developed by Shabaev and Efros [36] for ZB NRs. Predictions from this model are plotted in **Figure 2 (b)** where solid, dashed, and dotted lines represent strong, moderate, and weak transitions. The good qualitative agreement between experiment and theory has, in turn, enabled us to assign α, β, γ and δ to excitonic resonances with transitions denoted by term symbols originating in molecular physics.

We have previously suggested that α, β, and γ correspond to $1\Sigma_{1/2}1\Sigma_e$, $1\Sigma_{3/2}1\Sigma_e$, and $1\Sigma_{1/2}^{HH}1\Sigma_e$ respectively.[29] However, ambiguity exists about the actual identities of β and γ. Namely, for β, we have alternatively suggested that it could be $2\Sigma_{1/2}1\Sigma_e$.[29] This stems from $2\Sigma_{1/2}1\Sigma_e$'s close proximity to β as well as from the fact that it is formally allowed under parallel polarized excitation. By contrast, $1\Sigma_{3/2}1\Sigma_e$ is formally "bright" only under perpendicularly polarized excitation.[31] Complicating this, predicted $2\Sigma_{3/2}1\Sigma_e$ energies are nearly degenerate with those of $2\Sigma_{1/2}1\Sigma_e$ though, like $1\Sigma_{3/2}1\Sigma_e$, $2\Sigma_{3/2}1\Sigma_e$ is only formally active under perpendicularly polarized excitation. **Figure 2 (b)** illustrates predicted $1\Sigma_{3/2}1\Sigma_e$, $2\Sigma_{1/2}1\Sigma_e$ and $2\Sigma_{3/2}1\Sigma_e$ energies relative to β.

Subsequent single NW absorption polarization anisotropy experiments have suggested that $1\Sigma_{3/2}1\Sigma_e$ is β since it possesses a sizable transition probability relative to either $2\Sigma_{1/2}1\Sigma_e$ or $2\Sigma_{3/2}1\Sigma_e$ (see Appendix, **Figure 8**). Furthermore, its theoretically-derived absorption polarization anisotropies (ρ) qualitatively agree with those seen experimentally.[31] Theoretical ρ-

values are evaluated using $\rho = \left(|M^{||}|^2 - |M^{\perp}|^2\right)/\left(|M^{||}|^2 + |M^{\perp}|^2\right)$, where $|M^{||}|^2$ and $|M^{\perp}|^2$ are the squared transition matrix elements for parallel and perpendicularly polarized excitation respectively.[31]

Similar ambiguities exist with the assignment of γ given its close proximity to $1\Pi_{1/2}^{HH}1\Pi_e$ and $1\Pi_{3/2}1\Pi_e$. This is illustrated in **Figure 2 (b)**. Qualitative correlation between the absorption polarization anisotropies for these states with experimental ρ-values also suggest that γ could originate from a mixture of both $1\Pi_{1/2}^{HH}1\Pi_e$ and $1\Pi_{3/2}1\Pi_e$.[31] In general, though, the ZB model explains the coarse structure of the size-dependent transitions seen in our prior single CdSe NW absorption data.

At this point, what is notable is that the model *does not* predict a sizable Stokes shift in the emission from CdSe NWs. Namely, it suggests that their band edge absorption and emission originate from the same $1\Sigma_{1/2}1\Sigma_e$ (i.e. α) transition, irrespective of size. **Figure 2 (a)**, by contrast, clearly shows that both ensemble and single wire spectra exhibit sizable Stokes shifts with values on the order of ~30 meV. In particular, the ensemble data possesses a Stokes shift of 40 meV while the three single wire data exhibit shifts of 25 meV ($a \sim 4.1$ nm), 8 meV ($a \sim 3.5$ nm), and 48 meV ($a \sim 2.8$ nm). The latter single wire spectra thus establish that ensemble NW Stokes shifts observed here and in other CdSe wires[22,23] do not arise from ensemble averaging.

Even more intriguing is that the compiled single wire data in **Figure 2 (b)** suggests a size-dependence. Specifically, NWs appear to show decreasing Stokes shifts with decreasing radius. This is better illustrated in **Figure 3 (a)** where extracted single wire shifts are plotted as a function of radius. A link between $1\Sigma_{1/2}1\Sigma_e$ (α) energy and NW radius is made through a sizing curve compiled from ensemble literature data (see Appendix, **Figure 9**).[6,32,34,37]

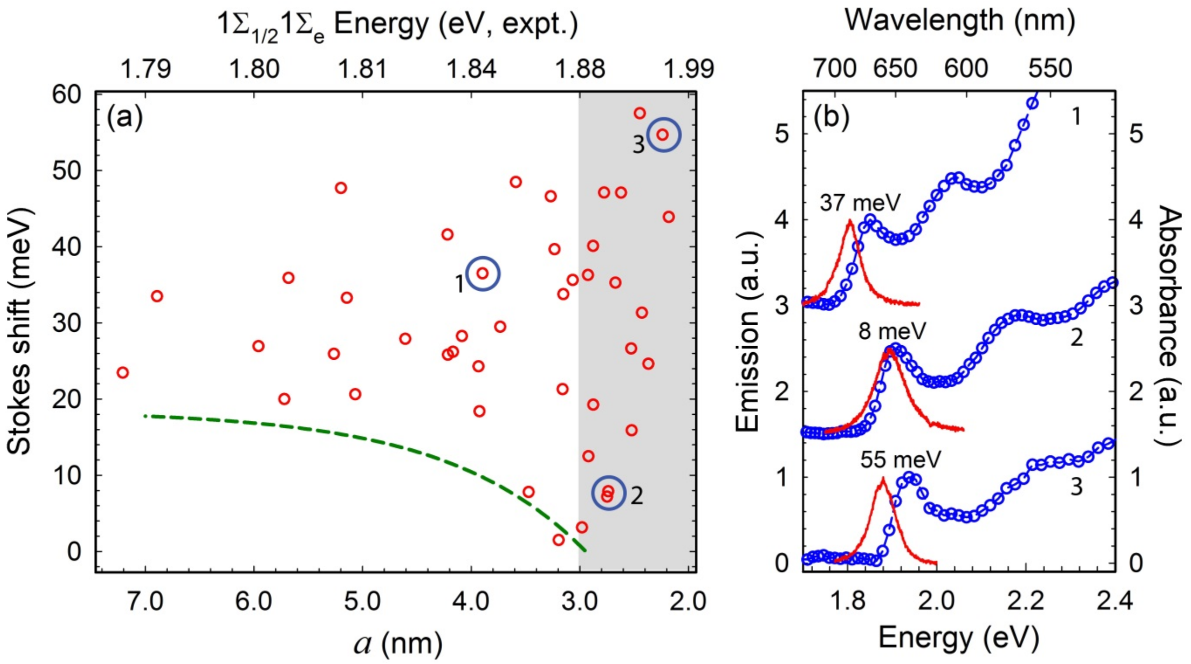

FIG. 3. (a) Plot of size-dependent single CdSe NW Stokes shifts. (b) Absorption/emission comparison of three wires from the circled points in (a). Data offset for clarity.

Figure 3 (a) first shows that NWs with $a > 4$ nm exhibit Stokes shifts that range from 20 to 50 meV. An average value is 29 meV (7.7 meV standard deviation). The lower left corner shows a dashed line below which no experimental Stokes shifts are observed. The origin of this line will be explained shortly. Next, as a decreases a subset of wires begin to exhibit smaller Stokes shifts. This culminates in the cluster of points near a~3 nm (1.88 eV), possessing near zero shifts. Finally, beyond 1.88 eV and denoted by the rightmost shaded region in **Figure 3 (a)** (a < 3 nm), most wires possess Stokes shifts > 20 meV. A general, upward trend can also be seen in the smallest NWs, despite the scatter in the data. **Figure 3 (b)** highlights this nonmonotonic Stokes shift behavior by showing absorption and emission spectra associated with the circled points in **Figure 3 (a)**.

III. MODIFICATIONS TO THEORY

The model we have previously used to assign transitions in the absorption of single CdSe NWs does not account for a significant emission Stokes shift. Although a small offset of ~1-2 meV is predicted due to fine structure in the $1\Sigma_{1/2}1\Sigma_{e}$ transition (resulting from the combined effects of crystal field splitting and the electron-hole exchange interaction[36]), such fine structure does not account for the 30-40 meV Stokes shifts seen in **Figures 2**, and **3**.

To reconcile this discrepancy, we note that CdSe NWs are not purely ZB. In fact, they contain ZB/W phase admixtures.[23] Thus, to account for the partial W character of the wires, we incorporate an effective crystal field splitting parameter directly into the Luttinger-Kohn Hamiltonian used to describe CdSe's valence band.[38] The approach follows similar work by Efros and Lambrecht[38] to explain observed emission polarization reversals seen in ZB and W GaAs/GaN NWs.[39]

The explicit introduction of crystal field splitting in the model does not affect CdSe's conduction band. Consequently, conduction band wavefunctions/energies are determined using a one band effective mass model. Resulting electron wavefunctions take the form

$$\psi^{e}_{n_e|m|} = \frac{u_{\pm 1/2}}{\sqrt{\pi}aJ'_{|m|}(\alpha_{n_e|m|})} J_{|m|}\left(\frac{\alpha_{n_e|m|}}{a}\rho\right) e^{im\phi} \tag{1}$$

where n_e is a quantum number representing the electron level, m is its angular momentum projection onto the NW z axis, a is the nanowire radius, $u_{\pm 1/2}$ is the electron Bloch function, $J_{|m|}(x)$ is the $|m|$-th order Bessel function, $J'_{|m|}(x)$ is its first derivative, $\alpha_{n_e|m|}$ is the Bessel function's n_e-th root, ρ is radius and ϕ is the azimuthal angle in cylindrical coordinates. Associated electron energies are

$$E_{n_e|m|} = \frac{\hbar^2 \alpha^2_{n_e|m|}}{2m(E_{n_e|m|})a^2} \tag{2}$$

where $m(E_{n_e|m|})$ is an energy-dependent effective mass (see Appendix). Each electron level is subsequently labelled $n_e\Lambda_e$, where Λ_e is a term symbol that denotes the state's angular momentum projection onto the NW z axis [i.e. Σ (m = 0), Π (m = 1), Δ (m = 2), etc…]. The lowest conduction band electron state is therefore $1\Sigma_e$.

Valence band levels are obtained by diagonalizing the modified Luttinger-Kohn Hamiltonian which incorporates the explicit crystal field splitting parameter, Δ (Δ = 25 meV[40]). In what follows, only four of six bands in CdSe are considered since its split-off hole band resides 420 meV above either the heavy or light hole bands. The resulting Hamiltonian written in the hole Bloch function basis $\left|\frac{3}{2},\frac{3}{2}\right\rangle, \left|\frac{3}{2},\frac{1}{2}\right\rangle, \left|\frac{3}{2},-\frac{1}{2}\right\rangle, \left|\frac{3}{2},-\frac{3}{2}\right\rangle$, is

$$H = \begin{pmatrix} P+Q-\frac{\Delta}{2} & L & M & 0 \\ L^* & P-Q+\frac{\Delta}{2} & 0 & M \\ M^* & 0 & P-Q+\frac{\Delta}{2} & -L \\ 0 & M^* & -L^* & P+Q-\frac{\Delta}{2} \end{pmatrix} \tag{3}$$

where the operators P, Q, L and M are expressed in terms of the momentum operators $p_{x,y,z} = -i\hbar\nabla_{x,y,z}$ as follows:

$$\begin{aligned} P &= \frac{\gamma_1^L}{2m_0}p^2 \\ Q &= \frac{\gamma^L}{2m_0}(p_\perp^2 - 2p_z^2) \\ L &= \frac{-i\sqrt{3}\gamma^L}{m_0}p_z p_- \\ M &= \frac{\sqrt{3}\gamma^L}{2m_0}p_-^2. \end{aligned} \tag{4a}$$

In these expressions, m_0 is the electron rest mass, γ^L and γ_1^L are energy-dependent Luttinger parameters (see Appendix for explicit expressions) and

$$
\begin{aligned}
p^2 &= p_x^2 + p_y^2 + p_z^2 \\
p_{\pm} &= p_x \pm i p_y \qquad (4b) \\
p_{\perp}^2 &= p_x^2 + p_y^2.
\end{aligned}
$$

Reducing Eq. 3 to block diagonal form (see Appendix) followed by subsequent diagonalization results in eigenfunctions composed of linear combinations of heavy and light hole-like Bloch functions (see Appendix). Associated eigenvalues are $\lambda = \epsilon\gamma_1^L \pm \sqrt{4(\epsilon\gamma^L)^2 - \gamma^L\epsilon\Delta + \frac{\Delta^2}{4}}$ where $\epsilon = \frac{\hbar^2 k_{h/lh}^2}{2m_0}$. These eigenvalues are subsequently inverted to obtain the following energy-dependent heavy and light hole-like wavevectors, k_h and k_{lh}

$$
k_h^2 = \frac{2m_0}{\hbar^2}\left[\frac{\gamma_1^L\lambda - \gamma^L\left(\frac{\Delta}{2}\right) + \sqrt{4{\gamma^L}^2\lambda^2 - \gamma_1^L\gamma^L\Delta\lambda + \left({\gamma_1^L}^2 - 3{\gamma^L}^2\right)\frac{\Delta^2}{4}}}{{\gamma_1^L}^2 - 4{\gamma^L}^2}\right] \qquad (5a)
$$

$$
k_{lh}^2 = \frac{2m_0}{\hbar^2}\left[\frac{\gamma_1^L\lambda - \gamma^L\left(\frac{\Delta}{2}\right) - \sqrt{4{\gamma^L}^2\lambda^2 - \gamma_1^L\gamma^L\Delta\lambda + \left({\gamma_1^L}^2 - 3{\gamma^L}^2\right)\frac{\Delta^2}{4}}}{{\gamma_1^L}^2 - 4{\gamma^L}^2}\right]. \qquad (5b)
$$

Incorporating corresponding envelope parts of the wavefunction leads to heavy and light hole –like Bloch wavefunctions, $\Psi_{h,F_z}^{\pm}$ and $\Psi_{lh,F_z}^{\pm}$ written as

$$
\begin{aligned}
\Psi_{h,F_z}^{\pm} &= C_1^{HH} J_{F_z \mp \frac{1}{2}}(k_h\rho) e^{i\left(F_z \mp \frac{1}{2}\right)\phi} \left|\frac{3}{2}, \pm\frac{1}{2}\right\rangle + C_2^{HH} J_{F_z \pm \frac{3}{2}}(k_h\rho) e^{i\left(F_z \pm \frac{3}{2}\right)\phi} \left|\frac{3}{2}, \mp\frac{3}{2}\right\rangle \\
\Psi_{lh,F_z}^{\pm} &= C_1^{LH} J_{F_z \mp \frac{1}{2}}(k_{lh}\rho) e^{i\left(F_z \mp \frac{1}{2}\right)\phi} \left|\frac{3}{2}, \pm\frac{1}{2}\right\rangle + C_2^{LH} J_{F_z \pm \frac{3}{2}}(k_{lh}\rho) e^{i\left(F_z \pm \frac{3}{2}\right)\phi} \left|\frac{3}{2}, \mp\frac{3}{2}\right\rangle.
\end{aligned} \qquad (6)
$$

Explicit expressions for the coefficients C_1^{LH}, C_2^{LH}, C_1^{HH}, and C_2^{HH} can be found in the Appendix. The + (–) superscript corresponds to solutions of the upper (lower) sub-block of the block diagonal form of Eq. 3 (see Appendix for block diagonal form) and F_z represents the hole's total angular momentum projection onto the NW z axis. Subsequently enforcing the system's radial boundary condition (i.e. the envelope part of the wavefunction equals zero when $\rho = a$) leads to desired hole wavefunctions, characterized by F_z, and composed of linear combinations of $\Psi_{h,F_z}^{\pm}$and $\Psi_{lh,F_z}^{\pm}$. The lowest energy hole states obtained are therefore doubly degenerate $|F_Z| = \frac{1}{2}$ and $\frac{3}{2}$ states. Corresponding wavefunctions for $|F_Z| = \frac{1}{2}$ are

$$\begin{aligned} \left|\uparrow_{1/2}\right\rangle &= a_{\uparrow_{1/2}} \left|\frac{3}{2}, \frac{1}{2}\right\rangle + b_{\uparrow_{1/2}} \left|\frac{3}{2}, -\frac{3}{2}\right\rangle \\ \left|\downarrow_{1/2}\right\rangle &= a_{\downarrow_{1/2}} \left|\frac{3}{2}, -\frac{1}{2}\right\rangle + b_{\downarrow_{1/2}} \left|\frac{3}{2}, \frac{3}{2}\right\rangle \end{aligned} \tag{7a}$$

with energy-dependent coefficients

$$\begin{aligned} a_{\uparrow_{1/2}} &= \frac{1}{\sqrt{2\pi N_{1/2}}} \left[C_1^{LH} J_0(k_{lh}\rho) - \left(\frac{C_2^{LH} J_2(k_{lh}a)}{C_2^{HH} J_2(k_h a)} \right) C_1^{HH} J_0(k_h \rho) \right] \\ b_{\uparrow_{1/2}} &= \frac{C_2^{LH} e^{2i\phi}}{\sqrt{2\pi N_{1/2}}} \left[J_2(k_{lh}\rho) - \left(\frac{J_2(k_{lh}a)}{J_2(k_h a)} \right) J_2(k_h \rho) \right] \\ a_{\downarrow_{1/2}} &= a_{\uparrow_{1/2}} \\ b_{\downarrow_{1/2}} &= b_{\uparrow_{1/2}}^{*}. \end{aligned} \tag{7b}$$

For $|F_Z| = \frac{3}{2}$, corresponding wavefunctions are

$$\begin{aligned} \left|\uparrow_{3/2}\right\rangle &= a_{\uparrow_{3/2}} \left|\frac{3}{2}, -\frac{1}{2}\right\rangle + b_{\uparrow_{3/2}} \left|\frac{3}{2}, \frac{3}{2}\right\rangle \\ \left|\downarrow_{3/2}\right\rangle &= a_{\downarrow_{3/2}} \left|\frac{3}{2}, \frac{1}{2}\right\rangle + b_{\downarrow_{3/2}} \left|\frac{3}{2}, -\frac{3}{2}\right\rangle \end{aligned} \tag{8a}$$

with associated energy-dependent coefficients

$$a_{\uparrow_{3/2}} = \frac{C_1^{HH} e^{2i\phi}}{\sqrt{2\pi N_{3/2}}}\left[J_2(k_h\rho) - \left(\frac{J_2(k_h a)}{J_2(k_{lh}a)}\right) J_2(k_{lh}\rho)\right]$$

$$b_{\uparrow_{3/2}} = \frac{1}{\sqrt{2\pi N_{3/2}}}\left[C_2^{HH} J_0(k_h\rho) - \left(\frac{C_1^{HH} J_2(k_h a)}{C_1^{LH} J_2(k_{lh}a)}\right) C_2^{LH} J_0(k_{lh}\rho)\right] \tag{8b}$$

$$a_{\downarrow_{3/2}} = a^*_{\uparrow_{3/2}}$$

$$b_{\downarrow_{3/2}} = b_{\uparrow_{3/2}}.$$

Expressions for the normalization constants $N_{1/2}$ and $N_{3/2}$ can be found in the Appendix. Associated energies for $|F_Z| = \frac{1}{2}$ and $\frac{3}{2}$ states are determined from solutions to the following characteristic equations:

$$C_1^{LH} C_2^{HH} J_0(k_{lh}a) J_2(k_h a) - C_1^{HH} C_2^{LH} J_0(k_h a) J_2(k_{lh}a) = 0 \qquad \left(|F_Z| = \tfrac{1}{2}\right) \tag{9a}$$

and

$$C_1^{LH} C_2^{HH} J_0(k_h a) J_2(k_{lh}a) - C_1^{HH} C_2^{LH} J_0(k_{lh}a) J_2(k_h a) = 0 \qquad \left(|F_Z| = \tfrac{3}{2}\right). \tag{9b}$$

Resulting hole states are then denoted using the term symbol $n_h \Lambda_{h_{F_z}}$ where n_h is the hole level of a given parity[4,29,36] and Λ_h arises from the smaller of $|m|$ and $|m+2|$—absolute values of the envelope angular momentum projection onto the NW z axis [i.e. Σ (*m* = 0), Π (*m* = 1), Δ (*m* = 2), etc…]. Term symbols for the doubly degenerate, even parity, $|F_Z| = \frac{1}{2}$ and $\frac{3}{2}$ states are therefore $1\Sigma_{1/2}$ and $1\Sigma_{3/2}$.

Calculated energies for band edge electron and hole levels are plotted in **Figure 4 (a)**. What is important is that the predicted size-dependent behavior of these hole levels differs from that in the ZB model. Namely, in the pure ZB case $1\Sigma_{1/2}$ is the lowest hole energy level for *all* NW sizes. Incorporating Δ into Eq. 3, however, results in $1\Sigma_{3/2}$ being the lowest hole state for *a* > 3 nm with a reversal of $1\Sigma_{3/2}$ and $1\Sigma_{1/2}$ energies at a ~ 3 nm. Consequently, for NWs with $a < 3$ nm, $1\Sigma_{1/2}$ is the lowest energy hole state. These model differences are shown explicitly in **Figure 10** of the Appendix.

At this point, to properly model NW optical transitions, Coulomb contributions to electron and hole energies must be explicitly considered. This includes direct interactions between charge carriers as well as self-interactions with image charges generated in the surrounding dielectric medium. Details about these calculations can be found in Refs. 4, 29, 36 and 41. When these electrostatic interactions are taken into account, we find that NW resonances (e.g. **Figure 2**) [4,29,36,41] are excitonic in nature with the lowest two band edge resonances of interest denoted as doubly degenerate $1\Sigma_{1/2}1\Sigma_e$ and $1\Sigma_{3/2}1\Sigma_e$ transitions.

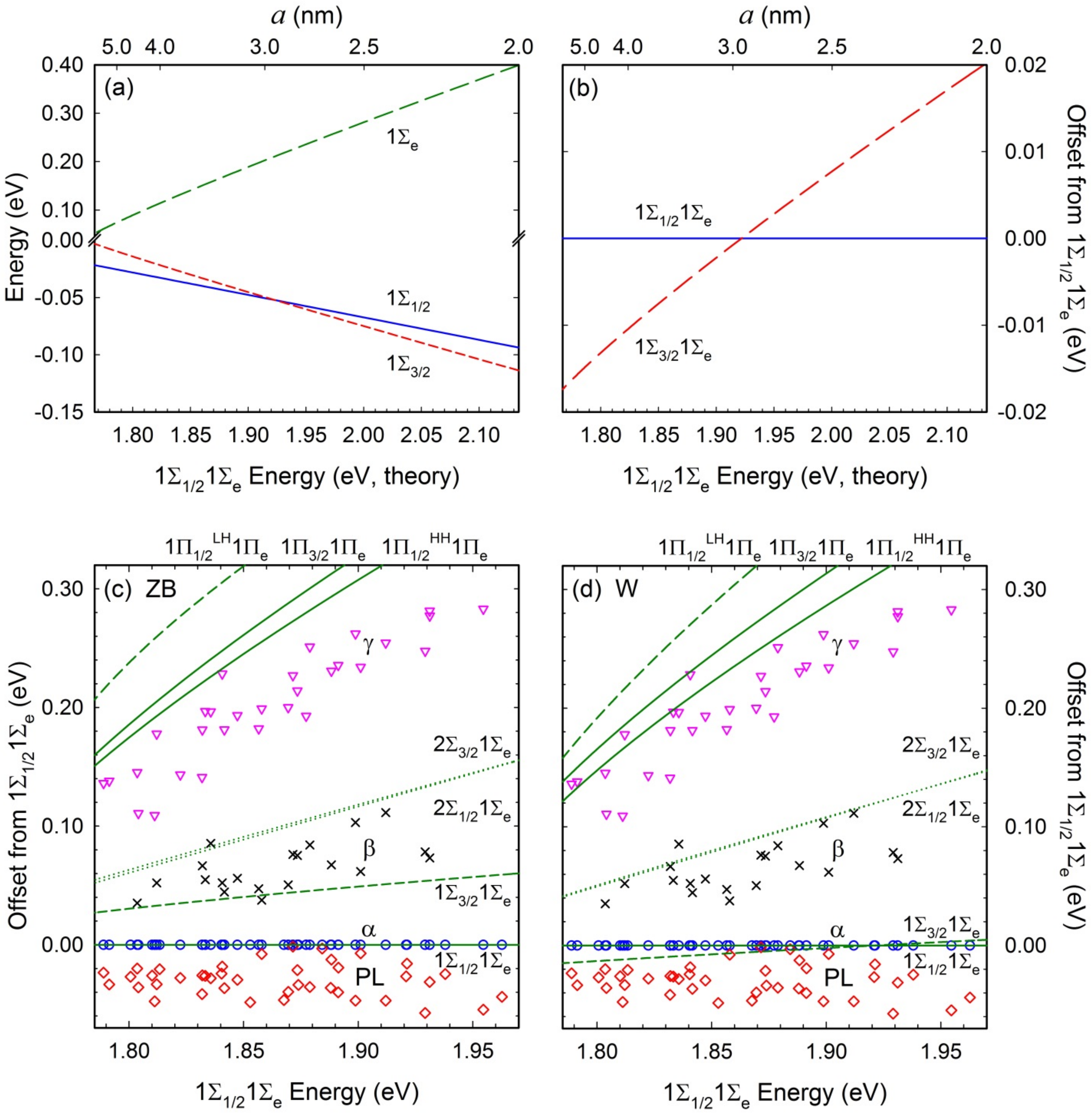

FIG. 4. (a) Band edge electron ($1\Sigma_e$) and hole ($1\Sigma_{1/2}$ and $1\Sigma_{3/2}$) energies. (b) Band edge excitonic energies plotted relative to the $1\Sigma_{1/2}1\Sigma_e$ energy. (c) ZB and (d) W model predictions for transition energies. The dielectric constants of the wire and the surrounding medium are assumed to be $\varepsilon_s = 6.1$ and $\varepsilon_m = 2.0$ respectively.

Figure 4 (b) shows calculated $1\Sigma_{1/2}1\Sigma_e$ and $1\Sigma_{3/2}1\Sigma_e$ energies plotted relative to the $1\Sigma_{1/2}1\Sigma_e$ energy. For NWs with $a < 3$ nm, the ground excitonic transition is $1\Sigma_{1/2}1\Sigma_e$ (solid blue curve). The next higher transition is $1\Sigma_{3/2}1\Sigma_e$ (dashed red curve). A crossing of the two levels occurs at

$a \sim 3$ nm and directly results from the hole state reversal in **Figure 4 (a)**. Consequently, for wires with $a > 3$ nm, $1\Sigma_{3/2}1\Sigma_e$ is the lowest predicted exciton transition.

We now highlight an important difference that arises between the predictions of the current (W) and former (ZB) models. **Figures 4 (c)** and **(d)** show the first few excitonic transitions in either model superimposed atop the experimental data. By comparing the two plots, it is immediately apparent that the main difference between the two models is their predicted $1\Sigma_{3/2}1\Sigma_e$ energies. In the W model, $1\Sigma_{1/2}1\Sigma_e$ and $1\Sigma_{3/2}1\Sigma_e$ are nearly superimposed and reverse order at $a \sim 3$ nm. By contrast, in the earlier ZB model, $1\Sigma_{1/2}1\Sigma_e$ and $1\Sigma_{3/2}1\Sigma_e$ are much further apart and never cross.

Beyond this, the effects of crystal field splitting are less important for higher excited states. **Figures 4 (c)** and **(d)** show that higher energy transitions (e.g. $2\Sigma_{1/2}1\Sigma_e$, $2\Sigma_{3/2}1\Sigma_e$, $1\Pi_{1/2}{}^{HH}1\Pi_e$, $1\Pi_{3/2}1\Pi_e$ and $1\Pi_{1/2}{}^{LH}1\Pi_e$) maintain the same ordering in either model. If anything, slight energy decreases occur for all transitions in the current model, bringing them in better agreement with the experimental data. Hence, only band edge states are strongly perturbed by the effects of crystal field splitting.

The lower overall energy of $1\Sigma_{3/2}1\Sigma_e$ and the reversal of $1\Sigma_{1/2}1\Sigma_e$ and $1\Sigma_{3/2}1\Sigma_e$ for $a > 3$ nm affect earlier assignments of CdSe NW excitonic transitions [**Figure 2 (b)**]. In this regard, β was previously attributed to $1\Sigma_{3/2}1\Sigma_e$. The current model, however, suggests that $1\Sigma_{3/2}1\Sigma_e$ is too low in energy to account for β. Instead, $2\Sigma_{1/2}1\Sigma_e$ and $2\Sigma_{3/2}1\Sigma_e$ are better suited for this. Of these two nearly degenerate states, only $2\Sigma_{1/2}1\Sigma_e$ is formally bright under parallel polarized excitation. $2\Sigma_{3/2}1\Sigma_e$ is active only when NWs are excited with perpendicularly polarized light. Theoretical transition probabilities for these two states are shown in **Figure 11** of the Appendix. From this perspective, it would therefore seem that β should be attributed to $2\Sigma_{1/2}1\Sigma_e$. However, our absorption polarization anisotropy experiments have also shown that β preferentially absorbs perpendicularly polarized light.[31] Hence, at this point, we attribute β to unresolved $2\Sigma_{1/2}1\Sigma_e$ and $2\Sigma_{3/2}1\Sigma_e$ transitions.

Next, we have previously attributed α to $1\Sigma_{1/2}1\Sigma_e$. However, **Figure 4 (d)** clearly shows that $1\Sigma_{1/2}1\Sigma_e$ and $1\Sigma_{3/2}1\Sigma_e$ are close in energy and within kT of each other at room temperature [**Figure 4 (b)**]. Consequently, given the resolution of room temperature single NW absorption measurements, it would appear that α consists of unresolved $1\Sigma_{1/2}1\Sigma_e$ and $1\Sigma_{3/2}1\Sigma_e$ transitions.

Some hints of this exist in the experimental data. Namely, **Figure 12 (**see Appendix) shows that only $1\Sigma_{1/2}1\Sigma_e$ is formally bright under parallel polarized excitation. By contrast, $1\Sigma_{3/2}1\Sigma_e$ is only active under perpendicularly polarized excitation.[31] Incorporating $1\Sigma_{3/2}1\Sigma_e$ into α would therefore mean that predicted absorption anisotropy values for this experimentally-observed transition should be smaller than those predicted by the pure ZB model—especially given that the ZB model considers α to be exclusively $1\Sigma_{1/2}1\Sigma_e$. In this regard, the W model predicts $\rho = 0.61$ to 0.85 (for ε_m values between 2 and 1) while the ZB model predicts $\rho = 0.88$ to 0.96 (for ε_m values between 2 and 1). Consequently, the W model is in better agreement with experimental α ρ-values, $\langle\rho\rangle = 0.86$.[31] Similarly, attributing β to overlapped $2\Sigma_{1/2}1\Sigma_e$ and $2\Sigma_{3/2}1\Sigma_e$ transitions leads to predicted ρ-values of $\rho = 0.38$ to 0.74 (for ε_m values between 2 and 1, $a = 3$ nm). This is again in better agreement with experimental β ρ-values of $\langle\rho\rangle = 0.62$, and is especially evident given that the ZB model predicts $\rho = -1$.[31]

Additionally, the close proximity of $1\Sigma_{1/2}1\Sigma_e$ and $1\Sigma_{3/2}1\Sigma_e$ is consistent with prior fine structure calculations conducted by Le Thomas *et al.* to explain unusual temperature-dependent lifetimes in CdSe NRs.[42] Namely, they observe increasing lifetimes with increasing temperature in narrow radii NRs with an opposite trend for larger radii NRs. A crossover in behavior occurs about a critical radius of 3.7 nm. This phenomenon is explained by a reversal of “bright” and “dark” exciton states, stemming from an analogous reversal of hole $S_{1/2}$ and $S_{3/2}$ states. Results of the current model are also consistent with pseudopotential calculation by Zhao *et al.* to model shape-dependent band edge electronic states of wurtzite CdSe nanocrystals.[43]

At this point, we conclude that α consists of unresolved $1\Sigma_{1/2}1\Sigma_e$ and $1\Sigma_{3/2}1\Sigma_e$ transitions. β is likewise attributed to unresolved $2\Sigma_{1/2}1\Sigma_e$ and $2\Sigma_{3/2}1\Sigma_e$ transitions. Assignment of γ remains ambiguous and, as described earlier, could arise due to $1\Pi_{1/2}^{HH}1\Pi_e$, $1\Pi_{3/2}1\Pi_e$ or a combination of these transitions. **Table 1** summarizes these revised assignments.

Table 1. Spectroscopic assignment of single CdSe NW optical transitions

Transition	ZB model	Current model
α	$1\Sigma_{1/2}1\Sigma_e$	$1\Sigma_{1/2}1\Sigma_e$ and $1\Sigma_{3/2}1\Sigma_e$
β	$1\Sigma_{3/2}1\Sigma_e$	$2\Sigma_{1/2}1\Sigma_e$ and $2\Sigma_{3/2}1\Sigma_e$
γ	$1\Pi_{1/2}^{HH}1\Pi_e$ and $1\Pi_{3/2}1\Pi_e$	$1\Pi_{1/2}^{HH}1\Pi_e$ and $1\Pi_{3/2}1\Pi_e$

Notably, apart from the above spectroscopic revisions, the model rationalizes the existence of a CdSe NW Stokes shift. Namely, because $1\Sigma_{1/2}1\Sigma_e$ is always the dominant absorbing state with parallel polarized light, it appears as α in **Figures 2, 4 (c) and 4 (d)**. Then despite being unresolved in α, $1\Sigma_{3/2}1\Sigma_e$ is the lowest excited state in $a > 3$ nm NWs. Consequently, exciton relaxation can occur into $1\Sigma_{3/2}1\Sigma_e$ and, in the absence of thermal repopulation of $1\Sigma_{1/2}1\Sigma_e$, leads to predicted Stokes shifts on the order of ~20 meV. The W model thus predicts an intrinsic Stokes shift, which is the difference in energy between $1\Sigma_{1/2}1\Sigma_e$ and $1\Sigma_{3/2}1\Sigma_e$ [**Figure 4 (b)**].

Next, **Figure 4 (b)** shows that as the NW radius decreases, the magnitude of this intrinsic shift approaches zero since $1\Sigma_{1/2}1\Sigma_e$ and $1\Sigma_{3/2}1\Sigma_e$ converge in energy and ultimately cross at $a \sim 3$ nm. No Stokes shift is therefore expected in $a < 3$ nm NWs. This intrinsic size-dependent

Stokes shift is highlighted by the dashed line first shown in **Figure 3 (a)**, which captures much of the qualitative behavior between a = 3 and 7 nm. Notably, the W model does not account for their absolute magnitudes or for the behavior seen in $a < 3$ nm NWs.

IV. EXCITON TRAP STATES

To explain quantitative discrepancies between experimental and theoretical Stokes shifts in $a > 3$ nm NWs and to explain the larger than expected values seen in narrow diameter wires, we invoke the role of exciton trap states. Namely, after excitation, we posit that photogenerated excitons thermalize into local potential energy minima, which reside *below* either $1\Sigma_{3/2}1\Sigma_e$ or $1\Sigma_{1/2}1\Sigma_e$ at the NW band edge. These states likely arise from incomplete organic ligand surface passivation,[44] or alternatively, stem from ZB/W phase admixtures previously shown to exist along the NW length.[23,33] In either case, the appearance of exciton traps contributes to the intrinsic shifts seen in **Figure 3 (a)** and leads to larger than expected NW Stokes shifts.

Such band edge potential energy fluctuations have previously been invoked to explain features seen in low temperature emission spectra of individual CdSe NWs. Specifically, an Urbach-like exponential tail of exciton trap states with a $1/e$ depth of ~18 meV has been used to explain the manifold of discrete (low temperature) resonances and low-energy (room temperature) spectral tails observed in CdSe NW emission spectra.[22] Although the corresponding emission polarization properties of these states are not known, they likely lead to emission polarized primarily along the wire's long axis given known NW dielectric properties.[25,45,46]

Qualitatively, the existence of such exciton traps with energies within the gap implies that subsequent emission will occur at energies lower than either $1\Sigma_{3/2}1\Sigma_e$ for $a > 3$ nm or $1\Sigma_{1/2}1\Sigma_e$

for $a < 3$ nm. In turn, experimental Stokes shifts will be larger than predicted and will reflect the energy separation between the dominant absorbing $1\Sigma_{1/2}1\Sigma_e$ state and these latter emitting, exciton trap states.

To model such trap-related contributions to the NW Stokes shift, we employ a framework previously used by Dunstan to explain the existence of apparent emission Stokes shifts in amorphous silicon.[47,48] The model first ascribes a probability $P_1 = e^{-\xi\epsilon}$ for an exciton to thermalize into a trap state with an energy, ϵ or greater, below the band edge. The parameter $\frac{1}{\xi}$ represents the average trap depth of the distribution. Next, the probability that this trap represents a local minimum surrounded by N nearest neighbors with larger energies is $P_2 = \left(1 - e^{-\xi\epsilon}\right)^N$.[47] Consequently, the joint probability that describes the likelihood of an exciton relaxing into an emitting, local minimum within the distribution is $P = P_1P_2 = \left(e^{-\xi\epsilon}\right)\left(1 - e^{-\xi\epsilon}\right)^N$.

Figure 13 of the Appendix plots P for various N values. In particular, it resembles an asymmetrically broadened Gaussian with a peak at

$$\epsilon_{max} = \frac{\ln(N+1)}{\xi}. \tag{10}$$

This energy is the most probable trap depth sampled by excitons within the distribution parameterized by N and $\frac{1}{\xi}$. Consequently, ϵ_{max} adds to the intrinsic Stokes shift between $1\Sigma_{1/2}1\Sigma_e$ and $1\Sigma_{3/2}1\Sigma_e$ for wires with $a > 3$ nm. For wires with $a < 3$ nm, it exclusively accounts for their Stokes shifts.

N represents the number of nearest neighbor—but higher energy—potential minima surrounding a given trap at ϵ. As such, it is ultimately linked to NW trap state densities (ρ_{trap}).

Prior studies have suggested ρ_{trap}-values of $\rho_{trap} \sim 1.3 \times 10^{19}$ cm^{-3} for CdSe NWs.[49,50] However, we know of no experiment that directly quantifies ρ_{trap} or which describes its size dependencies. Consequently, using $\rho_{trap} = 1 \times 10^{19}$ cm^{-3} and nominal NW dimensions of $a = 2 – 4$ nm and $l = 1$ μm, we estimate *upper limit* NW N-values ranging from $N = 1 – 6$. Additional details of this calculation can be found in the Appendix.

Figure 5 shows traces of expected Stokes shifts for trap distributions characterized by $N = 1$, 2, and 3 and $\frac{1}{\xi} = 18$ meV (dashed blue lines). The accompanying solid black line is the intrinsic Stokes shift predicted by theory [same trace shown in **Figure 3 (a)**]. Extrinsic trap state contributions thus readily add an additional ~ 12 – 25 meV to the theoretical shifts. Resulting intrinsic + extrinsic shifts consequently capture the overall magnitude of the experimental Stokes shift seen in $a \sim 3 – 7$ nm CdSe NWs.

More importantly, the apparent size-dependent behavior seen in **Figure 3 (a)** is also rationalized. Namely, the model suggests that a Stokes shift should *always* exist in larger diameter wires, with the intrinsic contribution representing a lower limit in $a > 3$ nm NWs. In this regard, what is notable in the experiment is that Stokes shifts significantly below the intrinsic theory line are never seen for $a \sim 3 – 7$ nm wires.

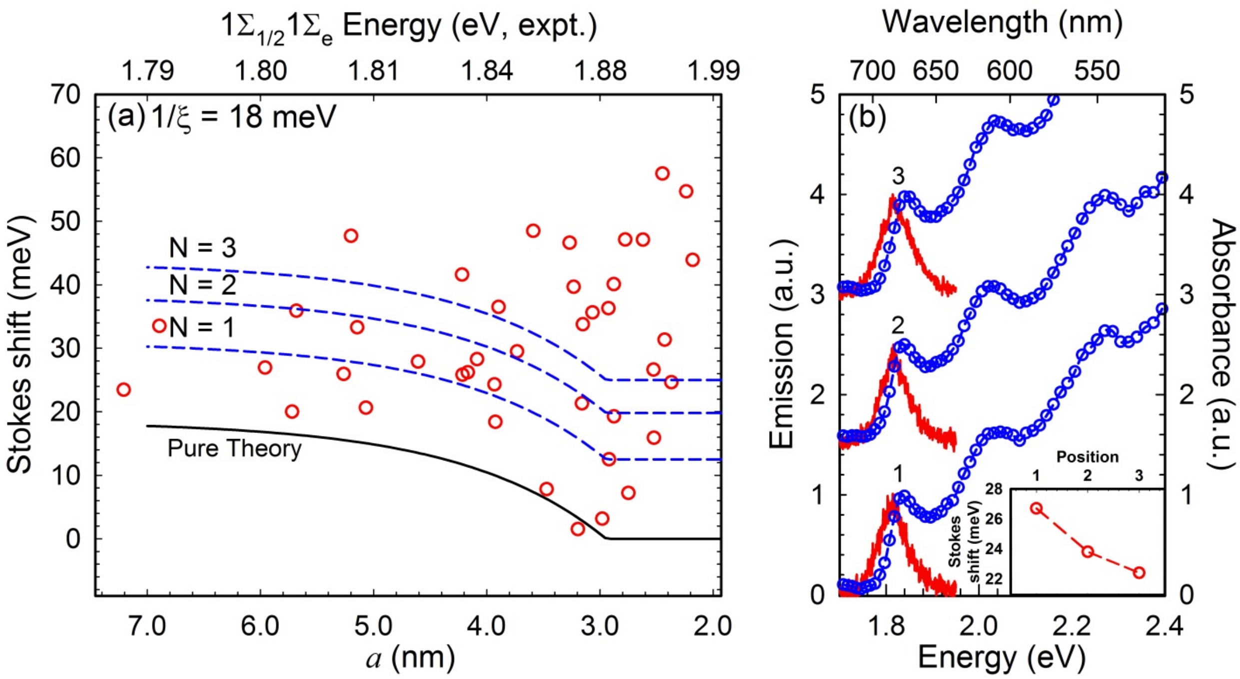

FIG. 5. (a) Plot of size-dependent single CdSe NW Stokes shifts (open red circles). Superimposed are predicted Stokes shifts, which contain intrinsic and extrinsic (*N*=1,2,3) contributions (dashed blue lines). The solid black line represents intrinsic shifts predicted by the W model. (b) Intrawire absorption (open blue circles) and emission (solid red lines) spectra taken from three different positions on a single *a* ~ 3.9 nm CdSe NW. The inset shows the associated Stokes shift for each position. Traces offset for clarity.

To further test this conclusion, we have conducted an additional single NW *intrawire* Stokes shift measurement by acquiring absorption and emission spectra from a single NW at different points across its length. The motivation for this stems from the possibility that spatial heterogeneities exist in the optical response of individual wires. Consequently, within the context of the current study, varying Stokes shifts, some smaller than the intrinsic theoretical limit, could potentially be averaged out in a single NW measurement which samples the wire's entire response.

Figure 5 (b) shows initial results from this study, conducted on a single *a* ~ 3.9 nm NW. Absorption and emission traces have been acquired at 3 points across the NW length, separated by ~1 μm. Analyzing resulting band edge absorption and emission energies subsequently leads to intrawire Stokes shifts, ranging from 22.4 to 26.7 meV. An average Stokes shift is 24.3 meV

(1.79 meV standard deviation). More relevantly, *none* of the measured shifts fall below the intrinsic theory limit shown in **Figure 5 (a)**. Thus, at this point, all of the experimental data corroborates predictions of the revised NW model described in Section III.

Finally, for NWs with $a < 3$ nm, no intrinsic contribution to the Stokes shift is predicted. Observed experimental shifts thus possess purely extrinsic origins. **Figure 5**, however, shows that the N = 1, 2, and 3 lines do not fully capture apparent trends in the data, namely, an increasing shift with decreasing size. Within the trap state analysis conducted, such an upwards trend can be rationalized if we assume that trap state densities arise, in part, from surface-related inhomogeneities/defects. This is because increasing the surface-to-volume ratio in narrow diameter wires leads to correspondingly larger trap densities and, by association, larger N-values. An upwards trend in NW Stokes shifts thus results if a size-dependent N parameter, varying inversely with NW radius (i.e. $N \propto \frac{1}{a}$), is assumed.

This assumption is not invoked, however, since the suggestion is highly speculative in the absence of additional information about NW trap state densities. Furthermore, there exist other possible reasons for larger than expected Stokes shifts in narrow radii NWs. For example, in the case where exciton fine structure exists, a small size-dependent contribution would add to the extrinsic shifts described above. Alternatively, we have previously observed that $a < 2.5$ nm NWs occasionally adopt $\langle 11\bar{2} \rangle$ growth directions.[34] Consequently, such wires could possess an electronic structure different from the [111]/[0001] oriented wires considered here. In this regard, a theoretical analysis of $\langle 11\bar{2} \rangle$ NWs is involved and is beyond the scope of the current study.

V. CONCLUSIONS

Concerted single CdSe NW absorption/emission spectroscopy has revealed, for the first time, the existence of sizable NW Stokes shifts. These shifts are not predicted by an existing effective mass theory previously used to explain size-dependent resonances in their linear absorption or in their associated absorption polarization anisotropies. Consequently, modifications to the theory have been carried out to properly account for the effects of crystal field splitting, especially on NW band edge states. In this way, we find that both the existence of CdSe NW Stokes shifts and their observed size-dependencies can be rationalized. The model, however, requires extrinsic, trap-related contributions to quantitatively explain their magnitudes.

In tandem, these modifications to theory have led to significant revisions to the predicted ordering of NW band edge states. This has required us to reassign experimental NW transitions. Namely, the ground exciton resonance (α) is now attributed to unresolved $1\Sigma_{3/2}1\Sigma_e$ and $1\Sigma_{1/2}1\Sigma_e$ transitions while β is likewise attributed to unresolved $2\Sigma_{1/2}1\Sigma_e$ and $2\Sigma_{3/2}1\Sigma_e$ transitions. This reassignment yields better quantitative agreement with experimental absorption polarization anisotropies and simultaneously rationalizes the existence of an emission Stokes shift. The use of concerted single nanostructure absorption and emission spectroscopy has therefore revealed detailed insights into the electronic structure of CdSe NWs beyond which could be obtained using more traditional ensemble and even single nanostructure spectroscopies.

ACKNOWLEDGEMENTS

We thank Andrew Shabaev and Alexander Efros for important conversations during this study. We also thank Pavel Frantsuzov for useful discussions during the writing of the manuscript. M. K. thanks the National Science Foundation (CHE 1208091) for financial support of this study.

APPENDIX

A. Synthesis and characterization of nanowire samples

1. $\langle a \rangle \sim 3.7$ nm NWs

CdO (25 mg, 0.19 mmol), myristic acid (0.331 g, 1.45 mmol) and trioctylphosphine oxide (1.5 g, 3.9 mmol) were mixed in a three-neck flask. The mixture was degassed at 100 °C for 50 minutes after which the temperature was raised to 250 °C under nitrogen. A solution of 1M trioctylphosphine selenide (25 μL, 25 μmol), 0.2 mL trioctylphosphine and 1 mM $BiCl_3$ in acetone (25 μL, 25 nmol) was then rapidly injected into this solution to initiate NW growth. The reaction was quenched through rapid cooling after 1 minute. The resulting suspension was subsequently centrifuged to recover the synthesized NWs. Excess surfactant was removed by washing the NW product 3-4 times with a 70:30 toluene:methanol mixture. Recovered NWs were subsequently stored in toluene. Representative low and high magnification TEM images are shown in **Figure 6**.

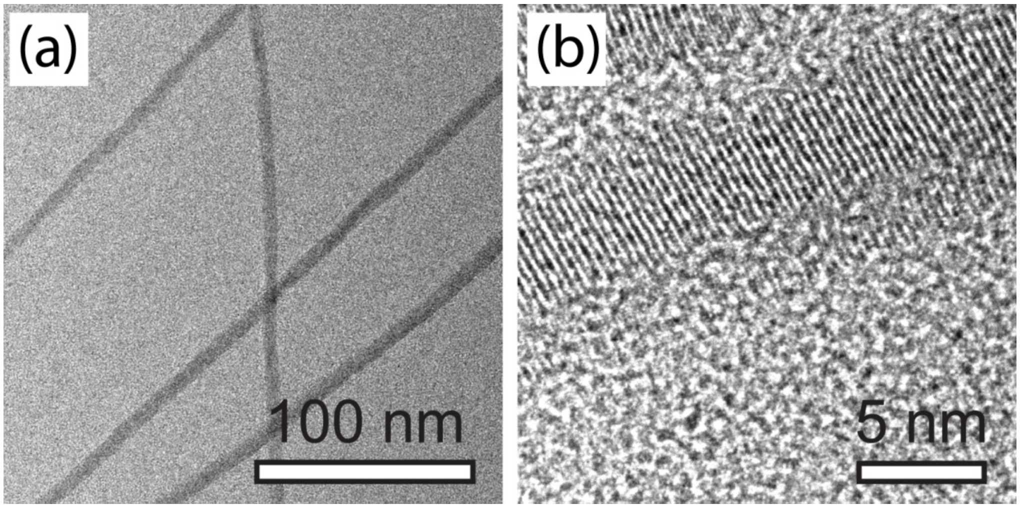

FIG. 6. (a) Low- and (b) high-magnification TEM images of an $\langle a \rangle \sim 3.7$ nm NW ensemble.

2. $\langle a \rangle \sim 5.0$ nm NWs

CdO (25 mg, 0.19 mmol), myristic acid (0.331 g, 1.45 mmol) and trioctylphosphine oxide (2.5 g, 6.5 mmol) were mixed in a three-neck flask. The mixture was degassed at 100 °C for 50 minutes after which the temperature was raised to 250 °C under nitrogen. A solution of 1M trioctylphosphine selenide (25 µL, 25 µmol), 0.2 mL trioctylphosphine and 2 mM $BiCl_3$ in acetone (60 µL, 120 nmol) was then rapidly injected to initiate NW growth. The reaction was allowed to proceed for 2 minutes before being quenched through rapid cooling. Resulting NWs were recovered by centrifuging the suspension. The recovered wires were subsequently purified by washing them 3-4 times with a 70:30 toluene:methanol mixture. Obtained NWs were stored in toluene. **Figure 7** shows representative low and high magnification TEM images of the sample.

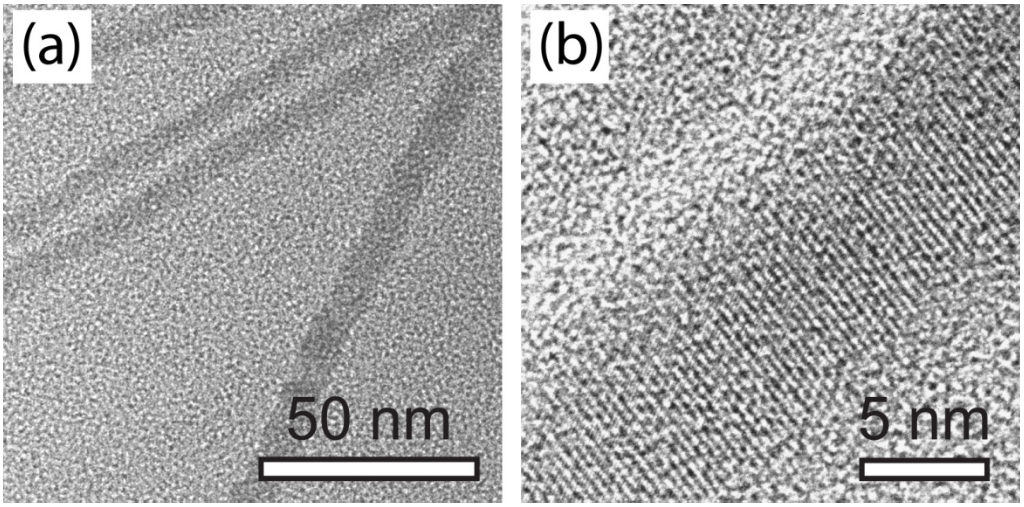

FIG. 7. (a) Low- and (b) high-magnification TEM images of an $\langle a \rangle \sim 5.0$ nm NW ensemble.

B. Transition matrix elements for possible β transitions (ZB model)

To help assign β, the following squared transition matrix elements ($|M|^2$) for $1\Sigma_{3/2}1\Sigma_e$, $2\Sigma_{3/2}1\Sigma_e$ and $2\Sigma_{1/2}1\Sigma_e$, were calculated using the ZB model.[31] Both parallel (||) and and perpendicular (⊥) polarized excitation were considered. $1\Sigma_{3/2}1\Sigma_e$ possesses the largest transition matrix element for perpendicularly polarized light. $2\Sigma_{3/2}1\Sigma_e$ and $1\Sigma_{3/2}1\Sigma_e$ are also inactive (i.e. $|M|^2=0$) under parallel polarized excitation.

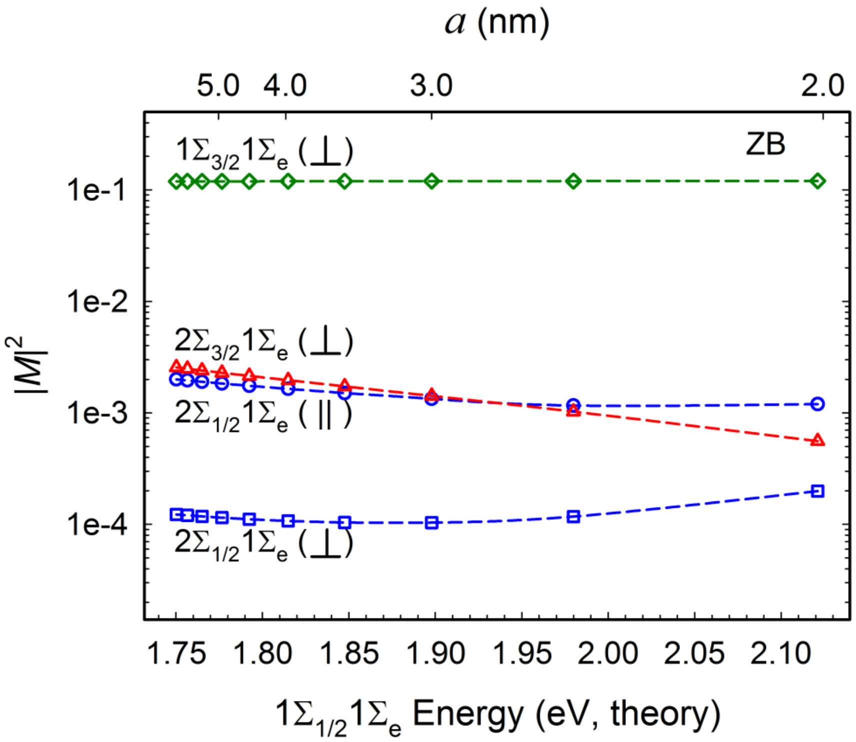

FIG. 8. Squared transition matrix elements for $1\Sigma_{3/2}1\Sigma_e$, $2\Sigma_{3/2}1\Sigma_e$ and $2\Sigma_{1/2}1\Sigma_e$ using the ZB model. Dielectric constants of the wire and the surrounding medium are assumed to be $\varepsilon_s = 6.1$ and $\varepsilon_m = 2.0$ respectively.

C. Sizing curve

A NW sizing curve has been constructed using ensemble literature data.[6,32,34,37] This sizing curve relates NW radii, *a*, to the band edge (α) transition energy.

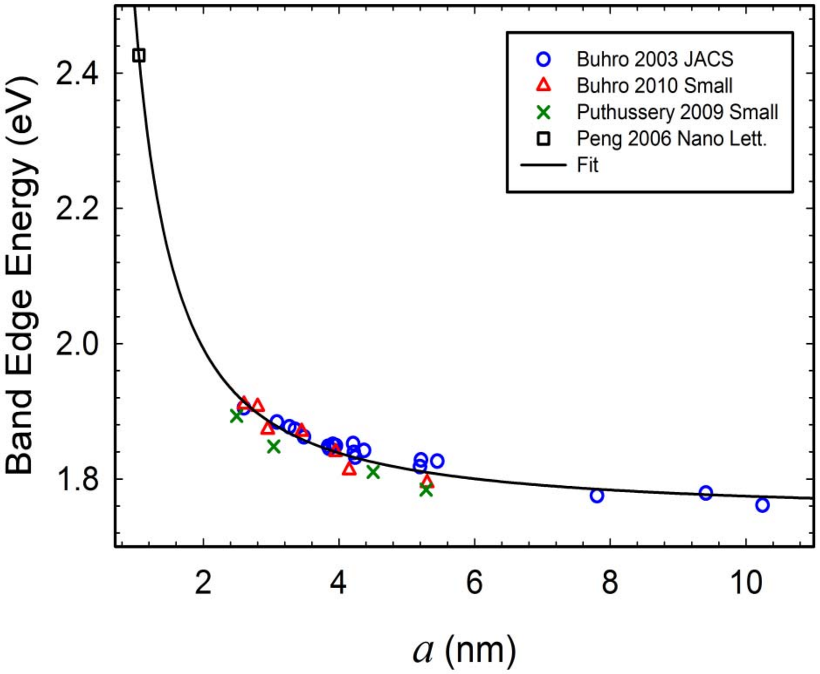

FIG. 9. Sizing curve correlating NW band edge (α) energy to radius.

The data is fit with the equation, $E_{band\ edge}(\text{eV}) = 1.7440 + \frac{0.2570}{a} + \frac{0.4802}{a^2}$ where a is in nm. Single NW radii are estimated from experimentally determined band edge energies by inverting this equation to yield $a(\text{nm}) = \frac{-0.2570-\sqrt{0.0660-1.9208[1.7440-E_{band\ edge}(\text{eV})]}}{2[1.7440-E_{band\ edge}(\text{eV})]}$.

D. Modified theory

1. Electron wavefunctions and energies

Electron wavefunctions and energies are obtained using a one-band effective mass model.[4,29,36] Explicit expressions for $\psi^{e}_{n_e|m|}$ and $E_{n_e|m|}$ are given by Eqs. 1 and 2 in the main text. The associated energy-dependent electron effective mass is

$$m(E_{n_e|m|}) = \frac{m_0}{1 + 2f + \frac{E_p}{3}\left(\frac{2}{E_{n_e|m|} + E_g} + \frac{1}{E_{n_e|m|} + E_g + \Delta_{SO}}\right)} \tag{A1}$$

and assumes $E_g = 1.74$ eV (the ZB band gap energy at 293 K), $\Delta_{SO} = 0.420$ eV (the spin-orbit splitting in CdSe), a Kane energy parameter of $E_p = 19$ eV and $f = -1.035$. The latter parameter accounts for remote band contributions. Wavefunctions are denoted by the term symbol $n_e\Lambda_e$, where n_e and Λ_e are described in the main text.

2. Hole wavefunctions and energies

The four band Hamiltonian for holes, which explicitly includes crystal field splitting, is given by Eqs. 3 and 4 of the main text. Employed energy-dependent Luttinger parameters are

$$\begin{aligned} \gamma^L(E) &= 0.54 - \frac{E_p}{6E_g} + \frac{E_p}{6(E_g + E)} \\ \gamma_1^L(E) &= 2.14 - \frac{E_p}{3E_g} + \frac{E_p}{3(E_g + E)}. \end{aligned} \tag{A2}$$

To further simplify Eq. 3, k_z and p_z are set to zero. This ignores longitudinal kinetic energy contributions to hole energies. Using $p_\pm = \pm i\hbar k$, $p_\perp = \hbar k$, and $\epsilon = \frac{\hbar^2 k^2}{2m_0}$ and re-ordering the basis to $\left|\frac{3}{2}, \frac{1}{2}\right\rangle, \left|\frac{3}{2}, -\frac{3}{2}\right\rangle, \left|\frac{3}{2}, -\frac{1}{2}\right\rangle, \left|\frac{3}{2}, \frac{3}{2}\right\rangle$, results in the following block-diagonal form

$$H = \begin{pmatrix} \epsilon(\gamma_1^L - \gamma^L) + \frac{\Delta}{2} & -\sqrt{3}\gamma^L\epsilon & 0 & 0 \\ -\sqrt{3}\gamma^L\epsilon & \epsilon(\gamma_1^L + \gamma^L) - \frac{\Delta}{2} & 0 & 0 \\ 0 & 0 & \epsilon(\gamma_1^L - \gamma^L) + \frac{\Delta}{2} & -\sqrt{3}\gamma^L\epsilon \\ 0 & 0 & -\sqrt{3}\gamma^L\epsilon & \epsilon(\gamma_1^L + \gamma^L) - \frac{\Delta}{2} \end{pmatrix}. \tag{A3}$$

Diagonalizing Eq. A3 yields the eigenvalues $\lambda = \epsilon\gamma_1^L \pm \sqrt{4(\epsilon\gamma^L)^2 - \gamma^L\epsilon\Delta + \frac{\Delta^2}{4}}$ with $\epsilon = \frac{\hbar^2 k_{h/lh}^2}{2m_0}$. $k_h$and k_{lh} (Eq. 5, main text) are subsequently found by inverting λ.

Corresponding eigenvectors are,

$$\Psi_{\lambda 1}^{\pm} = \begin{pmatrix} C_1^{LH} \\ C_2^{LH} \end{pmatrix} \tag{A4a}$$

$$\Psi_{\lambda 2}^{\pm} = \begin{pmatrix} C_1^{HH} \\ C_2^{HH} \end{pmatrix} \tag{A4b}$$

where the superscript + (–) represents solutions to the upper (lower) sub-block. The associated coefficients C_1^{LH}, C_2^{LH}, C_1^{HH}, C_2^{HH} are

$$C_1^{LH} = \frac{\sqrt{3}\gamma^L\epsilon_{lh}}{\sqrt{(\sqrt{3}\gamma^L\epsilon_{lh})^2 + \left(-\gamma^L\epsilon_{lh} + \frac{\Delta}{2} - \sqrt{4(\epsilon_{lh}\gamma^L)^2 - \gamma^L\epsilon_{lh}\Delta + \frac{\Delta^2}{4}}\right)^2}} \tag{A5a}$$

$$C_2^{LH} = \frac{-\gamma^L\epsilon_{lh} + \frac{\Delta}{2} - \sqrt{4(\epsilon_{lh}\gamma^L)^2 - \gamma^L\epsilon_{lh}\Delta + \frac{\Delta^2}{4}}}{\sqrt{(\sqrt{3}\gamma^L\epsilon_{lh})^2 + \left(-\gamma^L\epsilon_{lh} + \frac{\Delta}{2} - \sqrt{4(\epsilon_{lh}\gamma^L)^2 - \gamma^L\epsilon_{lh}\Delta + \frac{\Delta^2}{4}}\right)^2}} \tag{A5b}$$

$$C_1^{HH} = \frac{\sqrt{3}\gamma^L\epsilon_{h}}{\sqrt{(\sqrt{3}\gamma^L\epsilon_{h})^2 + \left(-\gamma^L\epsilon_{h} + \frac{\Delta}{2} + \sqrt{4(\epsilon_{h}\gamma^L)^2 - \gamma^L\epsilon_{h}\Delta + \frac{\Delta^2}{4}}\right)^2}} \tag{A5c}$$

$$C_2^{HH} = \frac{-\gamma^L\epsilon_{h} + \frac{\Delta}{2} + \sqrt{4(\epsilon_{h}\gamma^L)^2 - \gamma^L\epsilon_{h}\Delta + \frac{\Delta^2}{4}}}{\sqrt{(\sqrt{3}\gamma^L\epsilon_{h})^2 + \left(-\gamma^L\epsilon_{h} + \frac{\Delta}{2} + \sqrt{4(\epsilon_{h}\gamma^L)^2 - \gamma^L\epsilon_{h}\Delta + \frac{\Delta^2}{4}}\right)^2}}. \tag{A5d}$$

At this point, envelope functions associated with the Block functions are introduced. This yields Eq. 6 of the main text. Resulting functions $\Psi_{h,F_z}^{\pm}$ and $\Psi_{lh,F_z}^{\pm}$ are characterized by F_z, the total (Bloch + envelope) angular momentum projection onto the NW z-axis and are consistent with those of Efros,[36] Lambrecht[38] and Sercel and Vahala.[51,52]

Only hole functions of even parity are considered in what follows, given the electron's even parity envelope. Thus, only upper (lower) sub-block solutions, $\Psi^{+}_{h,1/2}$ and $\Psi^{+}_{lh,1/2}$ ($\Psi^{-}_{h,3/2}$ and $\Psi^{-}_{lh,3/2}$), are used for $F_z = \frac{1}{2}\left(\frac{3}{2}\right)$. Subsequently enforcing the NW's radial boundary condition yields NW hole wavefunctions which are linear combinations of $\Psi^{\pm}_{h,F_z}$ and $\Psi^{\pm}_{lh,F_z}$.

For $F_z = \frac{1}{2}$, the corresponding wavefunction, $\left|\uparrow_{1/2}\right\rangle$, is

$$\left|\uparrow_{1/2}\right\rangle = C_{LH}\Psi^{+}_{lh,1/2} + C_{HH}\Psi^{+}_{h,1/2}. \tag{A6a}$$

with weighting factors C_{HH} and C_{LH}. Written in terms of hole Bloch functions,

$$\boxed{\left|\uparrow_{1/2}\right\rangle = a_{\uparrow_{1/2}}\left|\frac{3}{2},\frac{1}{2}\right\rangle + b_{\uparrow_{1/2}}\left|\frac{3}{2},-\frac{3}{2}\right\rangle.} \tag{A6b}$$

with

$$a_{\uparrow_{1/2}} = C_{LH}C^{LH}_{1}J_0(k_{lh}\rho) + C_{HH}C^{HH}_{1}J_0(k_h\rho) \tag{A7}$$

$$b_{\uparrow_{1/2}} = C_{LH}C^{LH}_{2}J_2(k_{lh}\rho)e^{2i\phi} + C_{HH}C^{HH}_{2}J_2(k_h\rho)e^{2i\phi}.$$

Applying the radial boundary condition (i.e. $\left|\uparrow_{1/2}\right\rangle = 0$ when $\rho = a$) then results in the following characteristic equation whose roots are the energies of the $F_z = \frac{1}{2}$ state

$$C^{LH}_{1}C^{HH}_{2}J_0(k_{lh}a)J_2(k_ha) - C^{HH}_{1}C^{LH}_{2}J_0(k_ha)J_2(k_{lh}a) = 0. \tag{A8}$$

Given that the constraint also requires $a_{\uparrow_{1/2}} = 0$ and $b_{\uparrow_{1/2}} = 0$,

$$C_{HH} = -C_{LH}\frac{C^{LH}_{2}J_2(k_{lh}a)}{C^{HH}_{2}J_2(k_ha)}. \tag{A9}$$

Substituting Eq. A9 into Eq. A7 and normalizing the wavefunction (Eq. A6b) leads to explicit expressions for $a_{\uparrow_{1/2}}$ and $b_{\uparrow_{1/2}}$ which are shown as Eq. 7b in the main text. The associated normalization constant $N_{1/2}$ is

$$\begin{aligned}
&N_{1/2}\\
&= \frac{a^2}{2} {C_1^{LH}}^2 [J_0^2(k_{lh}a) + J_1^2(k_{lh}a)]\\
&- 2aC_1^{LH} C_1^{HH} \left(\frac{C_2^{LH} J_2(k_{lh}a)}{C_2^{HH} J_2(k_h a)}\right) \left(\frac{-k_h J_0(k_{lh}a) J_1(k_h a) + k_{lh} J_1(k_{lh}a) J_0(k_h a)}{{k_{lh}}^2 - {k_h}^2}\right)\\
&+ \frac{a^2}{2} \left(\frac{C_2^{LH} J_2(k_{lh}a)}{C_2^{HH} J_2(k_h a)}\right)^2 {C_1^{HH}}^2 [J_0^2(k_h a) + J_1^2(k_h a)] \qquad \text{(A10)}\\
&+ \frac{a^2}{2} {C_2^{LH}}^2 [J_2^2(k_{lh}a) - J_1(k_{lh}a) J_3(k_{lh}a)]\\
&- 2a{C_2^{LH}}^2 \left(\frac{J_2(k_{lh}a)}{J_2(k_h a)}\right) \left(\frac{-k_h J_2(k_{lh}a) J_1(k_h a) + k_{lh} J_1(k_{lh}a) J_2(k_h a)}{{k_{lh}}^2 - {k_h}^2}\right)\\
&+ \frac{a^2}{2} \left(\frac{J_2(k_{lh}a)}{J_2(k_h a)}\right)^2 {C_2^{LH}}^2 [J_2^2(k_h a) - J_1(k_h a) J_3(k_h a)].
\end{aligned}$$

Wavefunctions and energies for $F_z = -\frac{1}{2}$ and $F_z = \pm\frac{3}{2}$ states can be analogously determined. Resulting expressions are shown in Eqs. 7 – 9 of the main text. In this regard, the normalization constant, $N_{3/2}$, for $F_z = \pm\frac{3}{2}$ states is

$$\begin{aligned}
&N_{3/2} \\
&= \frac{a^2}{2} C_2^{HH^2} [J_0^2(k_h a) + J_1^2(k_h a)] \\
&- 2a C_2^{LH} C_2^{HH} \left(\frac{C_1^{HH} J_2(k_h a)}{C_1^{LH} J_2(k_{lh} a)} \right) \left(\frac{-k_h J_0(k_{lh} a) J_1(k_h a) + k_{lh} J_1(k_{lh} a) J_0(k_h a)}{{k_{lh}}^2 - {k_h}^2} \right) \\
&+ \frac{a^2}{2} \left(\frac{C_1^{HH} J_2(k_h a)}{C_1^{LH} J_2(k_{lh} a)} \right)^2 C_2^{LH^2} [J_0^2(k_{lh} a) + J_1^2(k_{lh} a)] \\
&+ \frac{a^2}{2} C_1^{HH^2} [J_2^2(k_h a) - J_1(k_h a) J_3(k_h a)] \\
&- 2a C_1^{HH^2} \left(\frac{J_2(k_h a)}{J_2(k_{lh} a)} \right) \left(\frac{k_h J_2(k_{lh} a) J_1(k_h a) - k_{lh} J_1(k_{lh} a) J_2(k_h a)}{{k_{lh}}^2 - {k_h}^2} \right) \\
&+ \frac{a^2}{2} \left(\frac{J_2(k_h a)}{J_2(k_{lh} a)} \right)^2 C_1^{HH^2} [J_2^2(k_{lh} a) - J_1(k_{lh} a) J_3(k_{lh} a)].
\end{aligned} \tag{A11}$$

Hole states are denoted by the term symbols $n_h \Lambda_{h_{F_z}}$, where n_h and $\Lambda_{h_{F_z}}$ have been described previously in the main text. Lowest energy $|F_z| = \frac{1}{2}$ and $\frac{3}{2}$ hole states are therefore represented by $1\Sigma_{1/2}$ and $1\Sigma_{3/2}$. **Figure 10 (a)** shows resulting $1\Sigma_{1/2}$ and $1\Sigma_{3/2}$ energies obtained using the current model. **Figure 10 (b)** shows corresponding energies calculated using the previous ZB model.[4,29] From a comparison of the two plots, $1\Sigma_{1/2}$ is the lowest energy hole state for all NW radii in the ZB model while in the W case $1\Sigma_{1/2}$ and $1\Sigma_{3/2}$ cross at *a* ~ 3 nm. Consequently, $1\Sigma_{3/2}$ is the lowest energy hole state for wires with $a > 3$ nm.

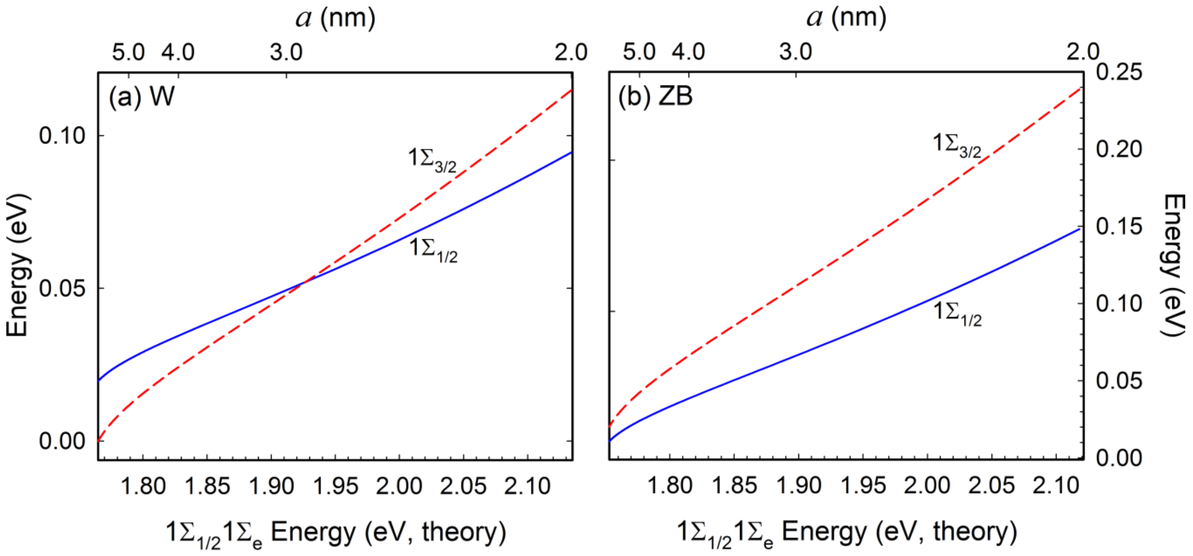

FIG. 10. Comparison of $|F_z| = \frac{1}{2}$ and $\frac{3}{2}$ hole energies in (a) ZB and (b) W CdSe NWs.

E. Transition probabilities and associated absorption polarization anisotropies

1. Transition probability calculation

Transition probabilities are estimated by evaluating the matrix element

$$\boxed{M = \langle \psi^{e}_{n_e \Lambda_e} | \boldsymbol{A} \cdot \hat{\boldsymbol{p}} | \psi^{h}_{n_h \Lambda_{h F_z}} \rangle} \tag{A12}$$

where $\boldsymbol{A}$ is the vector potential of the optical field and $\hat{\boldsymbol{p}}$ is the momentum operator. $\boldsymbol{A} \cdot \hat{\boldsymbol{p}}$ can be written as $A_0(\hat{\boldsymbol{e}} \cdot \hat{\boldsymbol{p}})$ where $A_0 = \frac{E_0}{\omega}$ for a monochromatic plane wave[53] and $\hat{\boldsymbol{e}}$ is a unit vector. To take the light's linear polarization into account, $\hat{\boldsymbol{e}} \cdot \hat{\boldsymbol{p}}$ is written as $\hat{\boldsymbol{e}}_z \cdot \hat{\boldsymbol{p}}_z + \hat{\boldsymbol{e}}_+ \cdot \hat{\boldsymbol{p}}_- + \hat{\boldsymbol{e}}_- \cdot \hat{\boldsymbol{p}}_+$ where

$$\begin{gathered} \hat{\boldsymbol{p}}_\pm = \frac{1}{\sqrt{2}}\left(\hat{\boldsymbol{p}}_x \pm i\hat{\boldsymbol{p}}_y\right) \\ \hat{\boldsymbol{e}}_\pm = \frac{1}{\sqrt{2}}\left(\hat{\boldsymbol{e}}_x \pm i\hat{\boldsymbol{e}}_y\right). \end{gathered} \tag{A13}$$

Eq. A12 then becomes

$$\boxed{M = \frac{E_0}{\omega}\left\langle \psi^e_{n_e\Lambda_e} \middle| \hat{\boldsymbol{e}}_{\boldsymbol{z}} \cdot \hat{\boldsymbol{p}}_{\boldsymbol{z}} + \hat{\boldsymbol{e}}_{+} \cdot \hat{\boldsymbol{p}}_{-} + \hat{\boldsymbol{e}}_{-} \cdot \hat{\boldsymbol{p}}_{+} \middle| \psi^h_{n_h\Lambda_{h_{F_z}}} \right\rangle.} \tag{A14}$$

For the $1\Sigma_{1/2}1\Sigma_e$ transition, the electron wavefunction, $\psi^e_{1\Sigma}$, is explicitly given by

$$|\psi^e_{1\Sigma}\rangle = \frac{J_0\left(\alpha_{10}\frac{\rho}{a}\right)}{\sqrt{\pi}aJ_0'(\alpha_{10})}|S\rangle = c|S\rangle \tag{A15}$$

where $|S\rangle$ is the electron's Bloch function, c is an even parity envelope function and spin up/down is implicitly assumed. The associated $F_z = \frac{1}{2}$ hole wavefunction is

$$\left|\uparrow_{1/2}\right\rangle = a_{\uparrow_{1/2}}\left|\frac{3}{2},\frac{1}{2}\right\rangle + b_{\uparrow_{1/2}}\left|\frac{3}{2},-\frac{3}{2}\right\rangle. \tag{A16}$$

Together with $|\psi^e_{1\Sigma}\rangle$ this yields the corresponding transition matrix element

$$M_{1/2} = \langle\psi^e_{1\Sigma}|\boldsymbol{A}\cdot\hat{\boldsymbol{p}}|\uparrow_{1/2}\rangle. \tag{A17}$$

When written out, $M_{1/2}$ becomes

$$\begin{aligned} M_{1/2} = \frac{E_0}{\omega}\Big[&\left\langle c\middle|a_{\uparrow_{1/2}}\right\rangle\left\langle S\middle|\hat{\boldsymbol{e}}_{\boldsymbol{z}} \cdot \hat{\boldsymbol{p}}_{\boldsymbol{z}} + \hat{\boldsymbol{e}}_{+} \cdot \hat{\boldsymbol{p}}_{-} + \hat{\boldsymbol{e}}_{-} \cdot \hat{\boldsymbol{p}}_{+}\middle|\frac{3}{2},\frac{1}{2}\right\rangle \\ &+ \left\langle c\middle|b_{\uparrow_{1/2}}\right\rangle\left\langle S\middle|\hat{\boldsymbol{e}}_{\boldsymbol{z}} \cdot \hat{\boldsymbol{p}}_{\boldsymbol{z}} + \hat{\boldsymbol{e}}_{+} \cdot \hat{\boldsymbol{p}}_{-} + \hat{\boldsymbol{e}}_{-} \cdot \hat{\boldsymbol{p}}_{+}\middle|\frac{3}{2},-\frac{3}{2}\right\rangle\Big] \end{aligned} \tag{A18}$$

where the second term in this expression vanishes since $\left\langle c\middle|b_{\uparrow_{1/2}}\right\rangle = 0$. Consequently,

$$M_{1/2} = \frac{E_0}{\omega}\left\langle c\middle|a_{\uparrow_{1/2}}\right\rangle\left\langle S\middle|\hat{\boldsymbol{e}}_{\boldsymbol{z}} \cdot \hat{\boldsymbol{p}}_{\boldsymbol{z}} + \hat{\boldsymbol{e}}_{+} \cdot \hat{\boldsymbol{p}}_{-} + \hat{\boldsymbol{e}}_{-} \cdot \hat{\boldsymbol{p}}_{+}\middle|\frac{3}{2},\frac{1}{2}\right\rangle. \tag{A19}$$

At this point, using[54]

$$\left|\frac{3}{2},\frac{1}{2}\right\rangle = \left|\frac{i}{\sqrt{6}}[(X+iY)\downarrow -2Z\uparrow]\right\rangle \tag{A20}$$

we obtain

$$M_{1/2} = \frac{E_0 i}{\omega\sqrt{6}}\left\langle c\middle|a_{\uparrow_{1/2}}\right\rangle\langle S|\hat{\boldsymbol{e}}_{\boldsymbol{z}} \cdot \hat{\boldsymbol{p}}_{\boldsymbol{z}} + \hat{\boldsymbol{e}}_{+} \cdot \hat{\boldsymbol{p}}_{-} + \hat{\boldsymbol{e}}_{-} \cdot \hat{\boldsymbol{p}}_{+}|(X+iY)\downarrow -2Z\uparrow\rangle. \tag{A21}$$

Finally, if the incident light is polarized parallel to the wire's z-axis, the transition matrix element $M_{1/2}^{\parallel}$ reduces to

$$M_{1/2}^{\parallel} = \frac{-2E_0 i}{\omega\sqrt{6}} \left\langle c \middle| a_{\uparrow_{1/2}} \right\rangle \langle S \uparrow | \hat{\boldsymbol{e}}_{\boldsymbol{z}} \cdot \hat{\boldsymbol{p}}_{\boldsymbol{z}} | Z \uparrow \rangle \tag{A22}$$

where $\langle S \uparrow | \hat{\boldsymbol{p}}_{\boldsymbol{z}} | Z \uparrow \rangle$ is the Kane matrix element (K_P) and $e_z \propto \cos\theta$, with θ the angle between the light polarization vector and the NW z axis. For $\theta = 0°$, we obtain

$$\boxed{\left| M_{1/2}^{\parallel} \right|^2 = \frac{2{K_P}^2}{3} \left(\frac{E_0}{\omega} \right)^2 \left| \left\langle c \middle| a_{\uparrow_{1/2}} \right\rangle \right|^2 .} \tag{A23}$$

Alternatively, if the light is polarized perpendicular to the NW z axis, the associated transition matrix element, $M_{1/2}^{\perp}$, is

$$\begin{aligned} M_{1/2}^{\perp} &= \frac{E_0 i}{\omega\sqrt{6}} \left\langle c \middle| a_{\uparrow_{\frac{1}{2}}} \right\rangle \langle S | \hat{\boldsymbol{e}}_+ \cdot \hat{\boldsymbol{p}}_- + \hat{\boldsymbol{e}}_- \cdot \hat{\boldsymbol{p}}_+ | (X + iY) \downarrow \rangle \left(\frac{2\varepsilon_m}{\varepsilon_m + \varepsilon_s} \right)^2 \\ &= \frac{E_0 i}{\omega\sqrt{6}} \left\langle c \middle| a_{\uparrow_{1/2}} \right\rangle \frac{e_+}{\sqrt{2}} \left(\langle S \downarrow | \hat{\boldsymbol{p}}_{\boldsymbol{x}} | X \downarrow \rangle + \langle S \downarrow | \hat{\boldsymbol{p}}_{\boldsymbol{y}} | Y \downarrow \rangle \right) \left(\frac{2\varepsilon_m}{\varepsilon_m + \varepsilon_s} \right)^2 . \end{aligned} \tag{A24}$$

with $\langle S \downarrow | \hat{\boldsymbol{p}}_{\boldsymbol{x}} | X \downarrow \rangle$ and $\langle S \downarrow | \hat{\boldsymbol{p}}_{\boldsymbol{y}} | Y \downarrow \rangle$ both Kane matrix elements (K_P), and ε_s and ε_m the dielectric constants for the wire and the surrounding medium respectively. Furthermore, $|e_+|^2 = \frac{|e_\perp|^2}{2} = \frac{\sin^2\theta}{2}$. Consequently, for $\theta = 90°$ we obtain

$$\boxed{\left| M_{1/2}^{\perp} \right|^2 = \frac{{K_P}^2}{6} \left(\frac{E_0}{\omega} \right)^2 \left| \left\langle c \middle| a_{\uparrow_{1/2}} \right\rangle \right|^2 \left(\frac{2\varepsilon_m}{\varepsilon_m + \varepsilon_s} \right)^2 .} \tag{A25}$$

Transition matrix elements for $1\Sigma_{3/2}1\Sigma_e$ are obtained analogously and are

$$\boxed{\begin{array}{l} \left| M_{3/2}^{\parallel} \right|^2 = 0 \\[2ex] \left| M_{3/2}^{\perp} \right|^2 = \dfrac{{K_P}^2}{2} \left(\dfrac{E_0}{\omega} \right)^2 \left| \left\langle c \middle| b_{\uparrow_{3/2}} \right\rangle \right|^2 \left(\dfrac{2\varepsilon_m}{\varepsilon_m + \varepsilon_s} \right)^2 . \end{array}} \tag{A26}$$

Expressions for $2\Sigma_{1/2}1\Sigma_e$ and $2\Sigma_{3/2}1\Sigma_e$ transition probabilities are derived in an identical manner using corresponding $2\Sigma_{1/2}$ and $2\Sigma_{3/2}$ hole state envelope functions.

Calculated squared transition matrix elements for $2\Sigma_{1/2}1\Sigma_e$ and $2\Sigma_{3/2}1\Sigma_e$ transitions are shown in **Figure 11**. The plot reveals that $2\Sigma_{1/2}1\Sigma_e$ possesses the largest overall transition probability under parallel polarized excitation. By contrast, $2\Sigma_{3/2}1\Sigma_e$ is dark under the same conditions. For perpendicularly polarized light, both $2\Sigma_{1/2}1\Sigma_e$ and $2\Sigma_{3/2}1\Sigma_e$ possess similar transition probabilities.

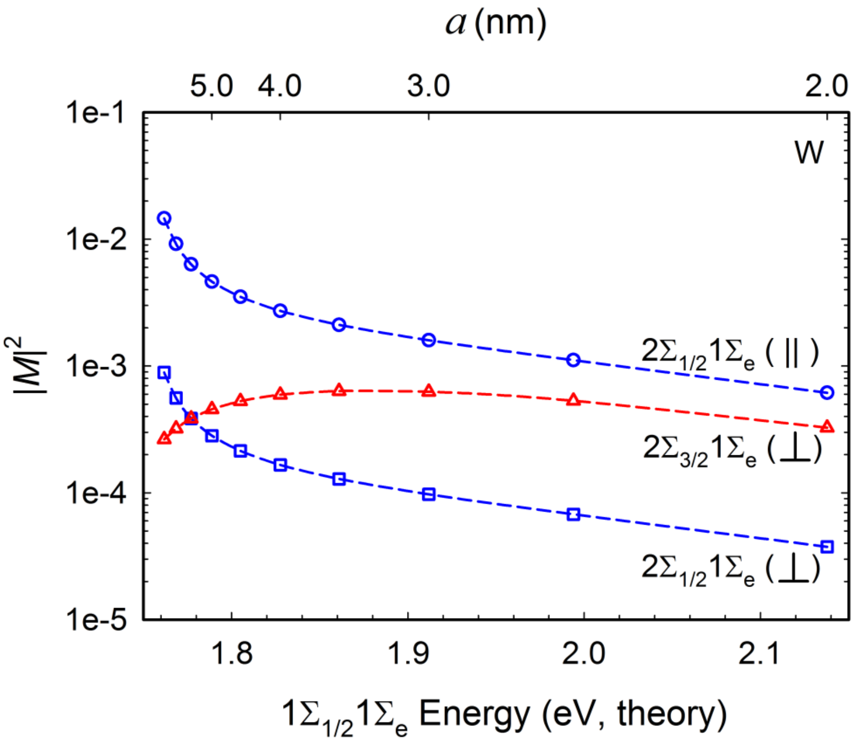

FIG. 11. Squared transition matrix elements for $2\Sigma_{1/2}1\Sigma_e$ and $2\Sigma_{3/2}1\Sigma_e$ under parallel (||) and perpendicularly (⊥) polarized excitation. Dielectric constants of the wire and the surrounding medium are assumed to be $\varepsilon_s = 6.1$ and $\varepsilon_m = 2.0$ respectively.

Analogous squared transition matrix elements for $1\Sigma_{1/2}1\Sigma_e$ and $1\Sigma_{3/2}1\Sigma_{e,}$ are shown in **Figure 12**. For parallel polarized light, $1\Sigma_{1/2}1\Sigma_e$ possesses the largest overall transition probability. $1\Sigma_{3/2}1\Sigma_e$ is dark under the same conditions. For perpendicularly polarized light, $1\Sigma_{3/2}1\Sigma_e$ possesses a transition probability larger than that for $1\Sigma_{1/2}1\Sigma_e$.

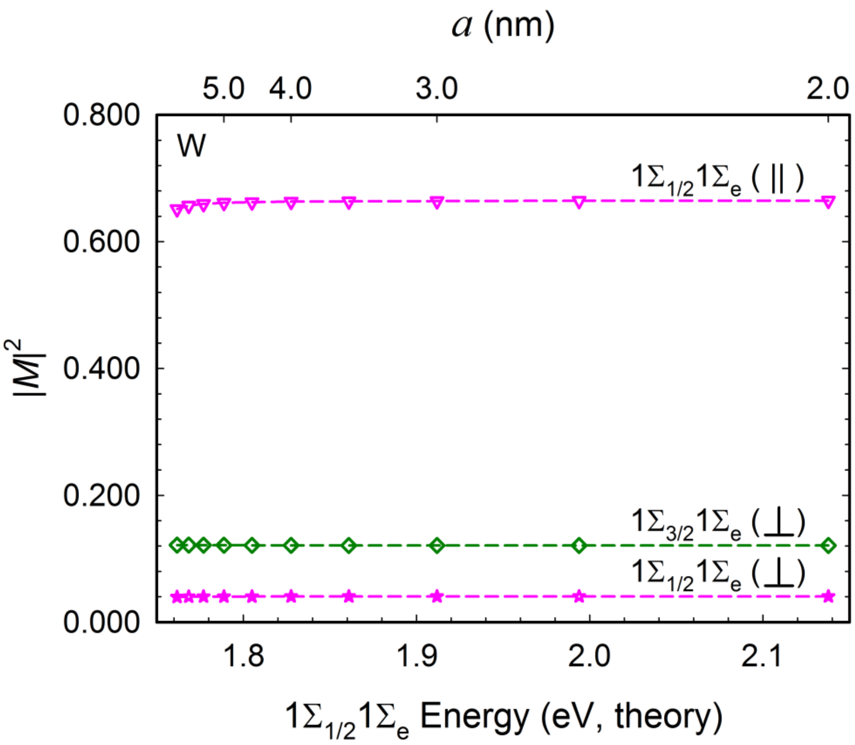

FIG. 12. Squared transition matrix elements for $1\Sigma_{1/2}1\Sigma_e$ and $1\Sigma_{3/2}1\Sigma_e$ under parallel (||) and perpendicularly (⊥) polarized excitation. Dielectric constants of the wire and the surrounding medium are assumed to be $\varepsilon_s = 6.1$ and $\varepsilon_m = 2.0$ respectively.

2. Calculation of effective absorption polarization anisotropies for overlapped transitions

The modified theory described above predicts that $1\Sigma_{1/2}1\Sigma_e$ and $1\Sigma_{3/2}1\Sigma_e$ possess similar energies [see **Figure 4 (d)**, main text]. Consequently, α likely represents an unresolved mixture of these two states. We thus model α's polarization parameter, ρ, using a composite anisotropy (ρ_c) given by

$$\rho_c = \frac{(|M_c^{\parallel}|^2 - |M_c^{\perp}|^2)}{\left(\left|M_c^{\parallel}\right|^2 + |M_c^{\perp}|^2\right)} \tag{A27}$$

where $|M_c^{\parallel}|^2$ and $|M_c^{\perp}|^2$ are composite squared transition matrix elements under parallel and perpendicularly polarized excitation. Specifically,

$$|M_c^{\parallel}|^2 = \left|M^{\parallel}_{1\Sigma_{1/2}1\Sigma_e}\right|^2 + \left|M^{\parallel}_{1\Sigma_{3/2}1\Sigma_e}\right|^2 \tag{A28}$$

and

$$|M_c^{\perp}|^2 = \left|M^{\perp}_{1\Sigma_{1/2}1\Sigma_e}\right|^2 + \left|M^{\perp}_{1\Sigma_{3/2}1\Sigma_e}\right|^2 \tag{A29}$$

for $1\Sigma_{1/2}1\Sigma_e$ and $1\Sigma_{3/2}1\Sigma_e$. Consequently, we find α absorption anisotropy values of $\rho_c = 0.61$ to 0.85 (for ε_m values between 2 and 1 and $\varepsilon_s = 6.1$).

The composite anisotropy value for β, which is attributed to unresolved $2\Sigma_{1/2}1\Sigma_e$ and $2\Sigma_{3/2}1\Sigma_e$ transitions, is likewise evaluated using

$$|M_c^{\parallel}|^2 = \left|M^{\parallel}_{2\Sigma_{1/2}1\Sigma_e}\right|^2 + \left|M^{\parallel}_{2\Sigma_{3/2}1\Sigma_e}\right|^2 \tag{A30}$$

and

$$|M_c^{\perp}|^2 = \left|M^{\perp}_{2\Sigma_{1/2}1\Sigma_e}\right|^2 + \left|M^{\perp}_{2\Sigma_{3/2}1\Sigma_e}\right|^2. \tag{A31}$$

For ε_m values between 2 and 1, $\varepsilon_s = 6.1$ and $a = 3$ nm, we find ρ_c-values ranging from $\rho_c = 0.38$ to 0.74.

F. Exciton trap states

As described in the main text, the probability for an exciton sampling a trap with an energy ϵ below the band edge is given by

$$P = \left(e^{-\xi\epsilon}\right)\left(1 - e^{-\xi\epsilon}\right)^N. \tag{A32}$$

The resulting distribution resembles an asymmetrically broadened Gaussian. It is illustrated below for different *N* values.

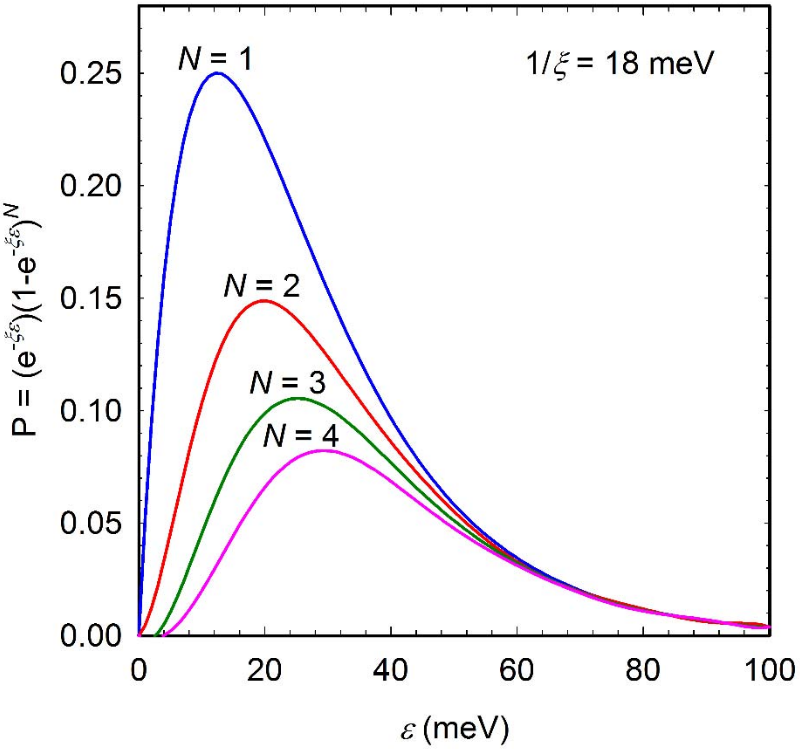

FIG. 13. Trap state probability distribution for $N = 1, 2, 3, 4$ and $1/\xi$=18 meV.

To estimate N, the number of traps an exciton samples within its Bohr radius is first evaluated. Assuming the bulk exciton Bohr radius of CdSe (a_B = 5.6 nm[15]), a trap density of $\rho_{\text{trap}} = 1 \times 10^{19}$ cm^{-3} and a NW length of l = 1 μm, we find

$$N = \rho_{\text{trap}}(2\pi a^2 a_B). \tag{A33}$$

Then, using a = 2 – 4 nm yields N values of N = 1 – 6. These values represent upper limits since actual localized exciton Bohr radii are likely to be smaller. Furthermore, a NW length of l=1 μm is assumed whereas experimental samples consist of wires with $l \gg 1$ μm.

REFERENCES

[1] S. V. Gaponenko, *Optical Properties of Semiconductor Nanocrystals* (Cambridge University Press, New York, 1998)

[2] M. A. Al-Sayed, Acc. Chem. Res. **37**, 326 (2004)

[3] M. Law, J. Goldberger and P. Yang, Annu. Rev. Mater. Res. **34**, 83 (2004)

[4] F. Vietmeyer, M. P. McDonald and M. Kuno, J. Phys. Chem. C **116**, 12379 (2012)

[5] M. Kuno, Phys. Chem. Chem. Phys. **10**, 620 (2008)

[6] H. Yu, J. Li, R. A. Loomis, P. C. Gibbons, L.-Wang and W. E. Buhro, J. Am. Chem. Soc. **125**, 16168 (2003)

[7] D. Franz, A. Reich, C. Strelow, Z. Wang, A. Kornowski, T. Kipp and A. Mews, Nano Lett. **14**, 6655 (2014)

[8] T. Schumacher, H. Giessen and M. Lippitz, Nano Lett. **13**, 1706 (2013)
[9] M. Law, L. E. Greene, J. C. Johnson, R. Saykally, and P. Yang, Nat. Mater. **4**, 455 (2005)

[10] Y. Yu, P. V. Kamat, and M. Kuno, Adv. Funct. Mater. **20**, 1464 (2010)

[11] H. Kind, H. Yan, B. Messer, M. Law and P. Yang, Adv. Mater. **14**, 158 (2002)

[12] W. U. Huynh, J. J. Dittmer and A. P. Alivisatos, Science **295**, 2425 (2002)

[13] J. Hu, L. Li, W. Yang, L. Manna, L. Wang and A. P. Alivisatos, Science **292**, 2060 (2001)

[14] Y. Huang, X. Duan and C. M. Lieber, Small **1**, 142 (2005)

[15] A. I. Ekimov, I. A. Kudryavtsev, Al. L. Efros, T. V. Yazeva, F. Hache, M. C. Schanne-Klein, A. V. Rodina, D. Ricard and C. Flytzanis, J. Opt. Soc. Am. B **10**, 100 (1993)

[16] D. J. Norris and M. G. Bawendi, Phys. Rev. B **53**, 16338 (1996)

[17] M. Kuno, J. K. Lee, B. O. Dabbousi, F. V. Mikulec and M. G. Bawendi, J. Chem. Phys. **106**, 9869 (1997)

[18] Al. L. Efros, M. Rosen, M. Kuno, M. Nirmal, D. J. Norris and M. Bawendi, Phys. Rev. B **54**, 4843 (1996)

[19] A. Hasselbarth, A. Echymuller and H. Weller, Chem. Phys. Lett. **203**, 271 (1993)

---

[20] M. G. Bawendi, P. J. Carroll, W. L. Wilson and L. E. Brus, J. Chem, Phys. **96**, 946 (1992)

[21] J. E. Boercker, E. M. Clifton, J. G. Tischler, E. E. Foos, T. J. Zega, M. E. Twigg and R. M. Stroud, J. Phys. Chem. Lett. **2**, 527 (2011)

[22] J. J. Glennon, R. Tang, W. E. Buhro, R. A. Loomis, D. A. Bussian, H. Htoon and V. I. Klimov, Phys. Rev. B **80**, 081303(R) (2009)

[23] V. V. Protasenko, K. L. Hull and M. Kuno, Adv. Mat. **17**, 2942 (2005)

[24] B. Lounis, H. A. Bechtel, D. Gerion, P. Alivisatos and W. E. Moerner, Chem. Phys. Lett. **329**, 399 (2000)

[25] A. Lan, J. Giblin, V. Protasenko and M. Kuno, Appl. Phys. Lett. **92**, 183110 (2008)

[26] C. Galland, S. Brovelli, W. K. Bae, L. A. Padilha, F. Meinardi and V. I. Klimov, Nano Lett. **13**, 321 (2013)

[27] V. Protasenko, D. Bacinello and M. Kuno, J. Phys. Chem. B **110**, 25322 (2006)

[28] J. Giblin, M. Syed, M. T. Banning, M. Kuno and G. Hartland, ACS Nano **4**, 358 (2010)

[29] J. Giblin, F. Vietmeyer, M. P. McDonald and M. Kuno, Nano Lett. **11**, 3307 (2011)

[30] M. P. McDonald, F. Vietmeyer, D. Aleksiuk and M. Kuno, Rev. Sci. Instrum. **84**, 113104 (2013)

[31] M. P. McDonald, F. Vietmeyer and M. Kuno, J. Phys. Chem. Lett. **3**, 2215 (2012)

[32] F. Wang and W. E. Buhro, Small **6**, 573 (2010)

[33] J. W. Grebinski, K. L. Hull, J. Zhang, T. H. Kosel and M. Kuno, Chem. Mater. **16**, 5260 (2004)

[34] J. Puthussery, T. H. Kosel and M. Kuno, Small **5**, 1112 (2009)

[35] Z. Wang, Z. Li, A. Kornowski, X. Ma, A. Myalitsin and A. Mews, Small **7**, 2464 (2011); Z. Li, O. Kurtulus, N. Fu, Z. Wang, A. Kornowski, U. Pietsch and A. Mews, Adv. Funct. Mat. **19**, 3650 (2009)

[36] A. Shabaev and Al. L. Efros, Nano Lett. **4**, 1821 (2004)

[37] N. Pradhan, H. Xu and X. Peng, Nano Lett. **6**, 720 (2006)

[38] Al. L. Efros and W. R. L. Lambrecht, Phys. Rev. B **89**, 035304 (2014)

[39] D. Spirkoska, Al. L. Efros, W. R. L. Lambrecht, T. Cheiwchanchamnangij, A. Fontcuberta i Morral and G. Abstreiter, Phys. Rev. B **85**, 045309 (2012)

[40] Al. L. Efros Phys. Rev. B **46**, 7448 (1992)

[41] A. C. Bartnik, Al. L. Efros, W. –K. Koh, C. B. Murray and F. W. Wise, Phys. Rev. B **82,** 195313 (2010)

[42] N. Le Thomas, E. Herz, O. Schöps, U. Woggon and M. V. Artemyev, Phys. Rev. Lett. **94**, 016803 (2005)

[43] Q. Zhao, P. A. Graf, W. B. Jones, A. Franceschetti, J. Li, L. Wang and K. Kim, Nano Lett. **7**, 3274 (2007)

[44] E. A. Muljarov, E. A. Zhukov, V. S. Dneprovskii and Y Masumoto, Phys. Rev. B **62**, 7420 (2000)

[45] H. E. Ruda and A. Shik, Phys. Rev. B **72**, 115308 (2005)

[46] G. Grzela, R. Paniagua-Dominguez, T. Barten, Y. Fontana, J. A. Sánchez-Gil and J. G. Rivas, Nano Lett. **12**, 5481 (2012)

[47] D. J. Dunstan, Solid State Commun. **43**, 341 (1982)

[48] F. Boulitrop and D. J. Dunstan, Phys. Rev. B **28**, 5923 (1983)

[49] J. J. Glennon, R. Tang, W. E. Buhro and R. A. Loomis, Nano Lett. **7**, 3290 (2007)

[50] J. J. Glennon, W. E. Buhro and R. A. Loomis, J. Phys. Chem. C **112**, 4813 (2008)

[51] P. C. Sercel and K. J. Vahala, Phys. Rev. B. **42**, 3690, (1990)

[52] P. C. Sercel and K. J. Vahala, Phys. Rev. B **44**, 5681 (1991)

[53] M. Kuno, *Introductory Nanoscience: Physical and Chemical Concepts* (Garland Science, New York, 2012)

[54] Al. L. Efros and M. Rosen, Annu. Rev. Mater. Sci. **30**, 475 (2000)